

## Controls on the termination of the massive chert system in the Ediacaran-Cambrian Liuchapo Formation, South China<sup>☆</sup>

Yuxuan Wang <sup>a</sup>, Fang Hao <sup>b</sup>, Yangbo Lu <sup>c,\*</sup>, Kaixun Zhang <sup>d</sup>, Yan Ye <sup>e</sup>, Shang Xu <sup>b,\*</sup>

<sup>a</sup> School of Earth and Environment, University of Leeds, Leeds LS2 9JT, UK

<sup>b</sup> State Key Laboratory of Deep Oil and Gas, China University of Petroleum (East China), Qingdao 266580, PR China

<sup>c</sup> School of Earth Resources, China University of Geosciences (Wuhan), Wuhan 430074, PR China

<sup>d</sup> Institute of Geomechanics, Chinese Academy of Geological Sciences, Beijing 100081, PR China

<sup>e</sup> Department of Geology, Lund University, Lund 22362, Sweden



### ARTICLE INFO

#### Keywords:

Chert  
Redox condition  
Ediacaran-Cambrian transition  
Liuchapo Formation

### ABSTRACT

The widespread deposition of marine siliceous rocks marks a fundamental shift in the ancient ocean's biogeochemical dynamics, transitioning from Precambrian systems dominated by direct inorganic silica precipitation as the primary silicon sink to modern environments where microbial processes strongly govern silica dissolution. The massive Liuchapo chert in the Nanhua Basin, South China, formed during the Ediacaran–Cambrian transition (ECT, ~550–521 Ma), a critical interval of silicon cycle perturbations, rapid multicellular diversification, and significant environmental change. Its abrupt termination, followed by the widespread deposition of Niutitang black shales without a depositional hiatus, reflects a fundamental shift in the oceanic silicon cycle, linked to profound marine environmental evolution and dynamic biotic responses during the key period of the ECT. However, the biogeochemical processes driving the cessation of chert deposition remain poorly understood. Here, we present high-resolution geochemical data from the XAD1 borehole, situated in an outer slope setting of the Nanhua Basin to assess controls on the termination of this widespread marine chert system. Our multi-proxy approach, including iron speciation, redox-sensitive trace metal analyses, and rare earth elements plus yttrium (REE + Y) systematics documents a highly fluctuated redox condition between oxic to ferruginous throughout the Liuchapo Formation, before giving way to persistent euxinic conditions in the lower Niutitang Formation. Hydrothermal activity likely played a key role in the Liuchapo chert formation, while its subsequent decline, coupled with the onset of euxinic conditions, weakened the Fe-Si loop essential for chert deposition. Furthermore, the emergence of silica-secreting organisms may have reduced dissolved silicon levels, further driving the cessation of chert deposition. These findings provide new insights into the environmental and biological factors controlling the termination of the Liuchapo massive chert system, contributing to a deeper understanding of the complex geochemical and ecological dynamics during this pivotal period in Earth's history.

### 1. Introduction

The marine dissolved silicon (Si) balance has exhibited distinct patterns throughout Earth's history. In modern oceans, silica is supplied through riverine input, aeolian dust, dissolution of continental margin sediments, and hydrothermal fluids, which collectively balance marine silica sinks through both biogenic and inorganic pathways (Baronas et al., 2017; Tréguer et al., 2021). Silica-secreting organisms (SSOs), such as diatoms and siliceous sponges, play a pivotal role in the modern marine Si cycle, accounting for nearly 100 % of silica precipitation in the

ocean (Tréguer et al., 2021). In the geological time, the transition from a Precambrian ocean saturated with inorganic Si to a Phanerozoic ocean undersaturated with Si is widely attributed to the evolutionary rise of SSOs and the associated reduction in dissolved Si availability (Maliva et al., 1989; Conley et al., 2017). This shift is supported by geological evidence, including changes in chert deposition patterns and the first widespread appearance of abundant SSO fossils in Phanerozoic strata (Maliva et al., 1989; Kidder and Erwin, 2001).

The Ediacaran-Cambrian transition represents a critical period in Earth's history, witnessing the emergence, extinction, and rapid

<sup>☆</sup> This article is part of a special issue entitled: 'Precambrian Evolution' published in Precambrian Research.

\* Corresponding authors.

E-mail addresses: [luyb@cug.edu.cn](mailto:luyb@cug.edu.cn) (Y. Lu), [xushang0222@163.com](mailto:xushang0222@163.com) (S. Xu).

diversification of multicellular organisms, alongside profound environmental shifts (Shields-Zhou and Zhu, 2013; Bowyer et al., 2024). During this period, the Liuchapo chert system, consisting of bedded cherts, was deposited in settings ranging from outer platform margins to deep basins within the Nanhua Basin, South China. These massive chert depositions exhibit remarkable continuity, with stratigraphic distribution of up to thousands of km<sup>2</sup> and thicknesses of up to 300 m in Guangxi Province (Chang et al., 2009; Dong et al., 2015). Comparable bedded chert deposits have been also documented globally in contemporaneous strata, such as the Yurtus Formation in the Tarim Block (Yu et al., 2009), the Ara Group in Oman (Ramseyer et al., 2013; Stolper et al., 2017), and the Tal Group in the Lesser Himalaya (Hughes et al., 2005), which represent a widespread perturbation of marine Si cycle around the ECT. The origins of the Liuchapo chert system have been the subject of debated, with conflicting hypotheses suggesting that the silica source originated either from continental weathering or hydrothermal fluids (Guo et al., 2007; Chang et al., 2009; He et al., 2013; Dong et al., 2015; Ramseyer et al., 2013; Tatzel et al., 2017; Ye et al., 2021; Li et al., 2022). During the Late Ediacaran, both intensified continental silicate weathering (Chang et al., 2009; Wei et al., 2024) and increased hydrothermal activity (Wang et al., 2011; Chang et al., 2020) coincided with the expansion of silica-secreting organisms (Ye et al., 2021; Zhang et al., 2021a,b), creating favorable conditions for widespread chert deposition (Braun and Chen, 2003; Guo et al., 2007). Notably, the termination of this extensive chert system in the Nanhua Basin was abrupt, marked by rapid transition to the deposition of Niutitang black shales without evidence of a depositional hiatus. This abrupt cessation may signify a major shift in the marine environmental conditions and ecosystem dynamic that has not been thoroughly addressed in studies of South China's deep-water systems during the ECT.

The dynamics of marine redox conditions during the ECT play a critical role in understanding environmental and biotic processes, significantly influencing chert deposition and subduction (Slack et al., 2007; Ling et al., 2013). However, due to the complexity of silica sources—including biotic activity, seawater precipitation, detrital input, and hydrothermal contributions during deposition, as well as potential remineralization during diagenesis—paleoenvironmental signals in chert samples must be interpreted with caution. For example, “anoxic” water column signal may be always occurred for pure chert (or carbonate) samples that imply a relatively low lithogenic fraction and hence a high biogenetic fraction, resulting in an evident high reactive iron concentration (Clarkson et al., 2014). Additionally, previous studies have predominantly focused on shallow-water carbonate platforms, leaving the deeper slope and basin settings under-explored. Furthermore, the role of biological evolution, particularly the emergence of silica-secreting organisms, in terminating large-scale chert systems remains unclear (Zhang and Shields, 2022).

To address this knowledge gap, we collected high-resolution borehole samples from the outer-slope XAD1 drill core, spanning the Liuchapo and Niutitang formations in the Nanhua Basin. This study examines the deposition and subsequent disappearance of the extensive Liuchapo chert system, reconstructing the redox history from the late Ediacaran to the early Cambrian in an outer-slope setting. Using a multi-proxy approach—including Fe speciation, redox-sensitive trace metals, REE + Y systematics, and sedimentological observations—we investigate the evolution of local redox conditions over short timescales and explore the mechanisms underlying the cessation of chert deposition. This comprehensive analysis provides new insights into the processes driving the termination of large-scale chert deposition and illuminates the broader environmental changes that defined this critical interval in Earth's history.

## 2. Geological setting

The South China Craton, composed of the Yangtze and Cathaysia blocks, underwent significant tectonic evolution during the

Neoproterozoic. These blocks amalgamated around 870 Ma and subsequently rifted from the supercontinent Rodinia approximately 800 Ma (Charvet, 2013). During this period, a rift system developed between the two blocks, eventually transitioning into a passive margin by the mid-Neoproterozoic (Zhang et al., 2015). By the early Cambrian, the craton had drifted to equatorial latitudes, with paleomagnetic data suggesting its connection to open oceans (Fig. 1A), a conclusion further supported by the presence of marine fossils (Liu et al., 2013).

During the early Fortunian Stage (~539 Ma), sedimentary environments across the craton transitioned from shallow-water platforms in the northwest to deep marine basins in the southeast, with an intervening transitional zone (Fig. 1B). The lithology across the Ediacaran–Cambrian boundary (ECB) reflects these depositional settings: gray dolomites and siliceous dolomites interbedded with chert characterize the Dengying and Yanjiahe formations in the northwest (Yunnan, Sichuan, and Hubei provinces), while black cherts and siliceous shales dominate the Liuchapo, Laobao, and Piyuancun formations in the southeast (Guizhou and Hunan provinces) (Wang et al., 2022). The ECB is marked by small shelly fauna (SSF1), trace fossils, and negative carbon isotope excursions (Goldberg et al., 2007), with volcanic ash layers occurring near the boundary in both the Liuchapo and Yanjiahe formations (Wang et al., 2022). By early Cambrian Stage 3 (~521 Ma), a global transgression and episodic hydrothermal activity submerged the carbonate platform, leading to the widespread deposition of organic-rich shales throughout South China (Wang et al., 2022). As sea levels fell during late Cambrian Stage 3 (~518 Ma), deposition in the Niutitang Formation shifted to gray shale and siltstone, reflecting a shallower depositional environment.

Our study focuses on the XAD 1 drillcore, located in an outer slope setting in the middle of Hunan Province, South China (Zhang et al., 2021a,b). The sampled borehole spans the late Ediacaran to early Cambrian strata, without any sedimentary hiatus. The lower Liuchapo Formation consists of siliceous shale at the base, transitioning to thick-bedded chert deposition in the upper portion. The Overlying Niutitang Formation is dominated by black, organic-rich shale with interbedded thin siliceous shale beds (Fig. 1C). Here, we draw on a SIMS U-Pb zircon age of 524.2 ± 5.1 Ma from the nearby Panmen section (0.45 m above the base of the Niutitang Formation, Fig. 1 C) to propose that the widespread lithofacies changes in South China were likely deposited around 20 million years after the onset of the Cambrian (Chen et al., 2015).

## 3. Materials and Methods

### 3.1. Samples

High-resolution sampling was conducted at the Xiangandi 1 Borehole. A total of 47 light to dark grey chert samples were collected from a depth range of 900 to 873 m within the lower Liuchapo Formation (Ediacaran–Cambrian). Another 10 samples of black shale, interbedded with thin cherty shale layers, were obtained from the 873 to 865 m depth of the uppermost Niutitang Formation (Cambrian) (Fig. 1C). Eleven polished thin sections were prepared for petrographic observation. Seven samples of different lithofacies, including chert, black shale, and siliceous shale, were also collected for X-ray powder diffraction (XRD) analysis. Prior to lab analysis, all weathered surfaces were removed. The geochemical analyses were performed at the State Key Laboratory of Biogeology and Environmental Geology, China University of Geosciences (Wuhan, China).

### 3.2. Total organic carbon (TOC), total sulfur (TS) and C<sub>org</sub> isotope

For the determination of TOC, sample powders were pretreated with 3 mol/L HCl and shaken overnight twice to remove carbonate phases. The residues were then rinsed at least three times with Milli-Q water to eliminate residual acid. Dried and regrinded samples were mixed with

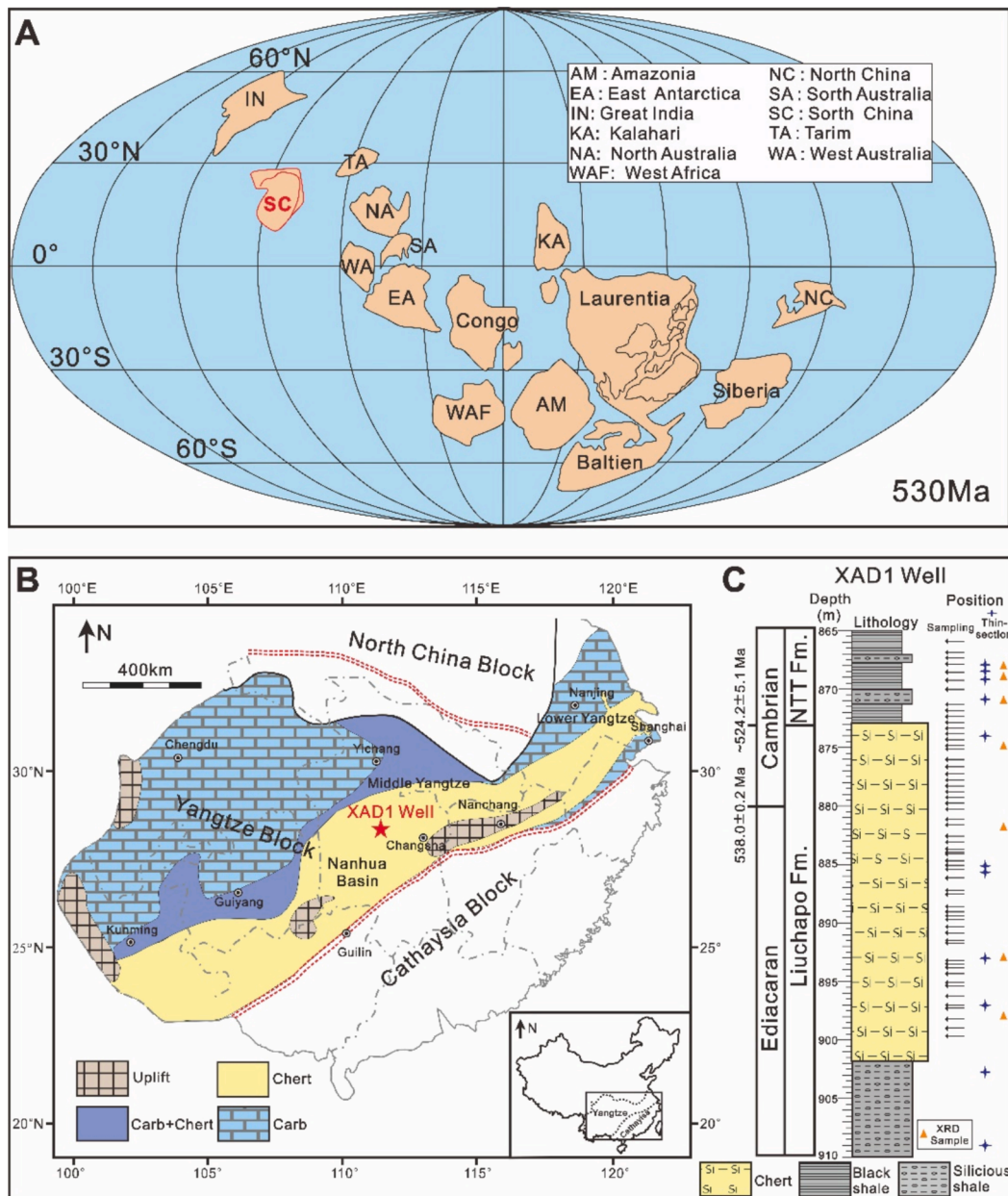


**Fig. 1.** Geological background and stratigraphic column of the XAD1 drill core, located in mid-Hunan Province, South China. (A) Global paleogeographic map at ~530 Ma, illustrating the tectonic context during the late Ediacaran-Cambrian transition, modified from Zhang et al., 2015. (B) Regional paleogeography of the Yangtze Block and the Nanhua Basin, showcasing depositional lithofacies during the Ediacaran-Cambrian transitional period, adapted from Jiang et al., (2011) and Chen et al. (2019). Black arrows indicate the positions of geochemical sampling; blue stars represent locations of thin section observations, while orange triangles denote samples selected for X-ray diffraction (XRD) analysis. The geochronology data for the South China Niutitang-Liuchapo Foramitum boundary is adapted from Chen et al., 2015.

tungsten trioxide as an accelerant, packed into tinfoil, and combusted at 1150 °C. The same procedure was applied for sulfur (TS) testing without acid treatment. The converted CO<sub>2</sub> and SO<sub>2</sub> were analyzed using a Vario Macro Cube elemental analyzer (Elementar, Hanau, German). Replicate analyses of certified standards gave a relative standard deviation (RSD) of < 5 %, and measurements were within 3 % of certified values. Approximately 0.5–5 mg of powder (~10 µg C) was placed in small tin capsules and combusted at 960 °C for separate C<sub>org</sub> measurements on a Flash HT 2000 Plus coupled to a continuous-flow Delta V Advantage IRMS (Thermo Fisher Scientific). Certified reference standards USGS24 (‰), USGS40 (‰) and IVA33802174 (‰) were analyzed together with unknowns for a multipoint calibration with an accuracy of better than 0.2 ‰ for <sup>13</sup>C<sub>org</sub>.

### 3.3. Iron speciation

Iron speciation was determined using a sequential extraction scheme for unsulfidized phases (Poulton and Canfield, 2005; Poulton, 2021), and a separate extraction scheme for Fe sulfides (Canfield et al., 1986). These techniques target Fe in carbonate phases (Fe<sub>carb</sub>), Fe (oxyhydr) oxides (Fe<sub>ox</sub>), magnetite Fe (Fe<sub>mag</sub>), and sulfide-bound Fe (Fe<sub>py</sub>), which together comprise highly reactive Fe (Fe<sub>HR</sub>). Sulfide-bound Fe, including acid volatile sulfide (Fe<sub>AVS</sub>; below detection in all cases) and pyrite (Fe<sub>py</sub>), was extracted using a two-step hydrochloric acid (HCl) and chromous chloride (CrCl<sub>2</sub>) technique (Canfield et al., 1986). The liberated H<sub>2</sub>S was collected as Ag<sub>2</sub>S, which was then determined gravimetrically and converted stoichiometrically to Fe<sub>py</sub> concentrations, with an

RSD of < 5 %. Unsulfidized Fe phases were determined via the sequential extraction scheme of Poulton and Canfield (2005). The Fe<sub>carb</sub> pool was extracted using Na-acetate solution at pH 4.5 and 50 °C for 48 h. The residue was then treated with Na-dithionite for 2 h at room temperature for determining the Fe<sub>ox</sub> phase. The last Fe<sub>mag</sub> phase was extracted with ammonium oxalate solution for 6 h at room temperature. All phases of dissolved Fe concentration were diluted and then identified by atomic absorption spectrometry (AAS). The replicate analysis ( $n = 8$ ) of the international reference material WHIT (Alcott et al., 2020) gave relative standard deviations (RSDs) < 5 % of all phases.

### 3.4. Bulk element concentrations

Approximately 50 mg of sample powder was weighed into a Teflon bomb and moistened with a few drops of ultrapure water, followed by the addition of 1 ml of HNO<sub>3</sub> and 1 ml of HF. The sealed bomb was then heated at 190 °C in an oven for over 48 h. After cooling, the bomb was opened, and the contents were evaporated at 115 °C to incipient dryness, followed by the addition of 1 ml of HNO<sub>3</sub> and a second evaporation to incipient dryness. The resultant salt was re-dissolved by adding 3 ml of 30 % HNO<sub>3</sub>, and the solution was resealed and heated in the bomb at 190 °C for over 12 h. Finally, the solution was transferred to a polyethylene bottle and diluted to approximately 100 g with a 2 % HNO<sub>3</sub> mixture. Total element concentrations were then analyzed via ICP-OES (ThermoFisher iCAP 7400) for major elements (Fe, Al, Mn) and ICP-MS (ThermoFisher iCAPQc) for trace element (U, Mo, REE + Y). Replicate extractions of international sediment standard SGR-1 yielded RSDs of < 5 % for all major and trace elements of interest, and analyses were within 5 % of certified values.

The enrichment factor (EF) for the redox sensitive elements is commonly used to assess the enrichment of redox sensitive elements compared to standards (e.g. Post-Archean Australian Average Shale, PAAS (Taylor and McLennan, 1985; McLennan, 2001), or other average shale compilations) in modern and ancient sediments (Tribouillard et al., 2006; Algeo & Li, 2020), and is generally calculated as:

$$X_{EF} = \frac{\left( \frac{X_{sample}}{Al_{sample}} \right)}{\left( \frac{X_{PAAS}}{Al_{PAAS}} \right)} \quad (1)$$

where X and Al denote the concentrations of element X and aluminum, respectively, in the sample. However, applying this method to (bio)chemical sediments, such as carbonates or cherts, can be problematic due to their low detrital Al content, which may lead to artificially high EF values compared to standard siliciclastic sediments (Tribouillard et al., 2006; Van der Weijden, 2002). Additionally, in typical siliciclastic sediments, elemental EF values can be quite low (less than 1) due to either low elemental background concentrations during a specific time period or the effects of bioturbation (Wang et al., 2024). Our trace data are all over PAAS values, so one solution is to consider excess element concentrations ( $X_{xs}$ ), which can be calculated as:

$$X_{excess} = X_{sample} - \left( Al_{sample} \times \left( \frac{X_{PAAS}}{Al_{PAAS}} \right) \right) \quad (2)$$

While useful, excess trace metal values lack direct comparability to standards, which can be critical for comparing to established techniques used for identifying different paleoredox conditions. So here we applied the modified element enrichment values (EF\*) (Krewer et al., 2024) calculated as:

$$X_{EF^*} = \frac{X_{excess} + X_{PAAS}}{X_{PAAS}} \quad (3)$$

This method maintains the straightness for comparison while also avoiding issues related to low detrital problems.

The rare earth elements (REEs) and Yttrium (Y) enrichment are standardized with PAAS values (subscript n represents shale normalization). To eliminate the interference of the relative enrichment of La and Gd elements in seawater and other natural water systems, the Ce and Eu anomalies values are calculated using the geometric series formula (Lawrence and Kamber, 2006):

$$Ce_n/Ce_n^* = Ce_n / \left( Pr_n \times \left( \frac{Pr_n}{Nd_n} \right) \right) \quad (4)$$

$$Eu_n/Eu_n^* = Eu_n / \left( \left( Sm_n^2 \times Tb_n \right)^{1/3} \right) \quad (5)$$

The magnitude of Ce and Eu anomalies is generally quantified as values < 1 for the negative Ce and Eu anomalies (indicating Ce and Eu depletion) and > 1 for the positive anomalies (indicating Ce and Eu enrichment).

### 3.5. Framework for redox interpretations

To reconstruct water column redox conditions, we utilized independent inorganic redox proxies based on Fe speciation and redox sensitive trace metal concentrations (including REE). Fe speciation uses the ratio of Fe<sub>HR</sub> to total Fe (Fe<sub>T</sub>) to infer redox conditions during deposition (Poulton, 2021; Poulton & Canfield, 2005, 2011). Modern and ancient calibrations provide general thresholds for identifying oxic versus anoxic environments (Raiswell and Canfield, 1998; Raiswell et al., 2001, 2018; Poulton and Raiswell, 2002; Poulton and Canfield, 2011; Clarkson et al., 2014; Poulton, 2021). Typically, Fe<sub>HR</sub>/Fe<sub>T</sub> ≤ 0.22 signals oxic conditions, while Fe<sub>HR</sub>/Fe<sub>T</sub> ≥ 0.38 indicates anoxic conditions due to additional Fe<sub>HR</sub> precipitation in the water column (Poulton & Canfield, 2005). Intermediate ratios (0.22–0.38) are ambiguous and require supplementary evidence for redox interpretation (Poulton & Canfield, 2011). In anoxic samples, the ratio of Fe<sub>py</sub>/Fe<sub>HR</sub> helps distinguish between euxinic (sulfidic) and ferruginous (Fe-rich) conditions. Fe<sub>py</sub>/Fe<sub>HR</sub> ratios above 0.6–0.8 generally reflect euxinia (Anderson and Raiswell, 2004; März et al., 2008; Benkovitz et al., 2020), while ratios ≤ 0.6 suggest ferruginous settings (Poulton & Canfield, 2011; Poulton, 2021). However, particular care needs to be taken when Fe speciation is applied to sediments with low total Fe contents (<0.5 wt%, Fe<sub>T</sub>), because non siliciclastic sediments (e.g., carbonate and chert) may give spuriously high Fe<sub>HR</sub>/Fe<sub>T</sub> ratios with limited detrital Fe source (Clarkson et al., 2014).

Uranium (U) and molybdenum (Mo), both highly soluble in oxic seawater, exhibit limited enrichment in oxic sediments (Morford et al., 2009). In oxygenated conditions, U predominantly exists as U(VI) in uranyl carbonate complexes (UO<sub>2</sub>(CO<sub>3</sub>)<sub>3</sub><sup>4-</sup>) (Calvert and Pedersen, 1993), while molybdenum is stable as Mo (VI) in the molybdate oxy-anion (MoO<sub>4</sub><sup>2-</sup>) (Zheng et al., 2000). When anoxia develops around the sediment–water interface, soluble U(VI) is reduced to insoluble U(IV), primarily at the Fe(II)–Fe(III) redox boundary (Anderson et al., 1989). In contrast, Mo removal needs the specific presence of relatively high HS<sup>-</sup> concentrations, where molybdenum forms thiomolybdate species (MoO<sub>x</sub>S<sub>4</sub><sup>x-</sup>) under euxinic conditions (Helz et al., 1996; Zheng et al., 2002).

Dissolved REEs in seawater are transferred into sediments through sorption to particles (e.g., Fe/Mn oxides, organic matter, silica) or by substituting Ca<sup>2+</sup> in carbonate and phosphate minerals, with bulk carbonates, iron formations, phosphorites, and cherts often preserving seawater-like REE patterns, making them useful proxies for the ancient redox reconstruction in these chemical depositions (German and Elderfield, 1990; Murray, 1992; Webb and Kamber, 2000; Bekker et al., 2014; Zhang and Shields, 2022). Particulate organic matter and iron and manganese (oxyhydr)oxides serve as the primary carriers of REEs, with light REEs (LREEs) mainly due to the discrepancy in stabilities of carbonate complexations in seawater (Sholkovitz et al., 1994; Schijf and Byrne, 2021). This differential scavenging induces fractionation among

REEs, resulting in the depletion of LREEs in oxic seawater (Sholkovitz et al., 1994). Cerium (Ce) and Europium (Eu) are unique among REEs due to their commonly multivalent property. While Eu (III) is reduced to Eu (II) predominantly under subsurface conditions during magmatic and hydrothermal processes (Bau, 1991), Ce demonstrates more dynamic redox behaviour in surface environments. Soluble Ce (III) tends to adsorb onto Fe and/or Mn (oxyhydr)oxide minerals, where it undergoes oxidation to the highly insoluble Ce (IV) in the oxygenated seawater column, leading to significant Ce depletion relative to neighboring REEs (De Baar et al., 1985; Sholkovitz et al., 1994; Bau and Koschinsky, 2009). As a result, oxic marine particulates generally exhibit higher LREE/HREE ratios and smaller negative or positive Ce anomalies compared to ambient oxic seawater. In contrast, under suboxic or anoxic conditions, particulate Mn, Fe, and Ce undergo reductive dissolution, releasing scavenged Ce into the water column and generating less HREE enrichment with smaller negative or even positive Ce anomalies in anoxic waters (German et al., 1991; Bau et al., 1997; Tostevin et al., 2016).

Thus, the combined analysis of REE patterns, U and Mo systematics, and Fe speciation can differentiate between oxic, anoxic non-sulfidic (ferruginous), and euxinic conditions. However, due to the distinct lithological transitions between the geochemical deposition of Liuchapo chert and the detrital Niutitang black shale, Fe speciation is a more reliable indicator of redox conditions in black shale and siliceous shale,

while Ce anomalies are more effective for chert systems.

## 4. Results

### 4.1. Lithofacies and mineral composition

In the study interval of the XAD 1 well, three primary lithofacies were identified: chert, siliceous shale, and black shale. The Liuchapo Formation chert is dominated by bedded chert structures, featuring small white quartz/carbonate veins (Fig. 2A; Table 1). Microscopically, these cherts are composed of bedded microcrystalline quartz and organic matter, with macrocrystalline quartz and coarse quartz crystals occasionally present throughout the sedimentary layers (Fig. 2D, E, F). Near the base of the Liuchapo chert at approximately 902 m, well-developed framboids were observed (Fig. 2G). Conversely, the Niutitang black shales primarily consist of diffused organic matter, amorphous biogenic silica, and some detrital microcrystalline quartz (Fig. 2B, H). The siliceous shales display an interbedded structure of black shale and bedded microcrystalline quartz (Fig. 2C, I).

X-ray diffraction analysis revealed that the quartz content in the Liuchapo chert samples averages 92.6 %, with minimal feldspar (<5%), carbonate (<5%), and clay (~0.5 %) (Table 3). The Niutitang black shales consist predominantly of quartz (>50 %) and clay minerals (~20–30 %), with smaller amounts of potassium feldspar, calcite,

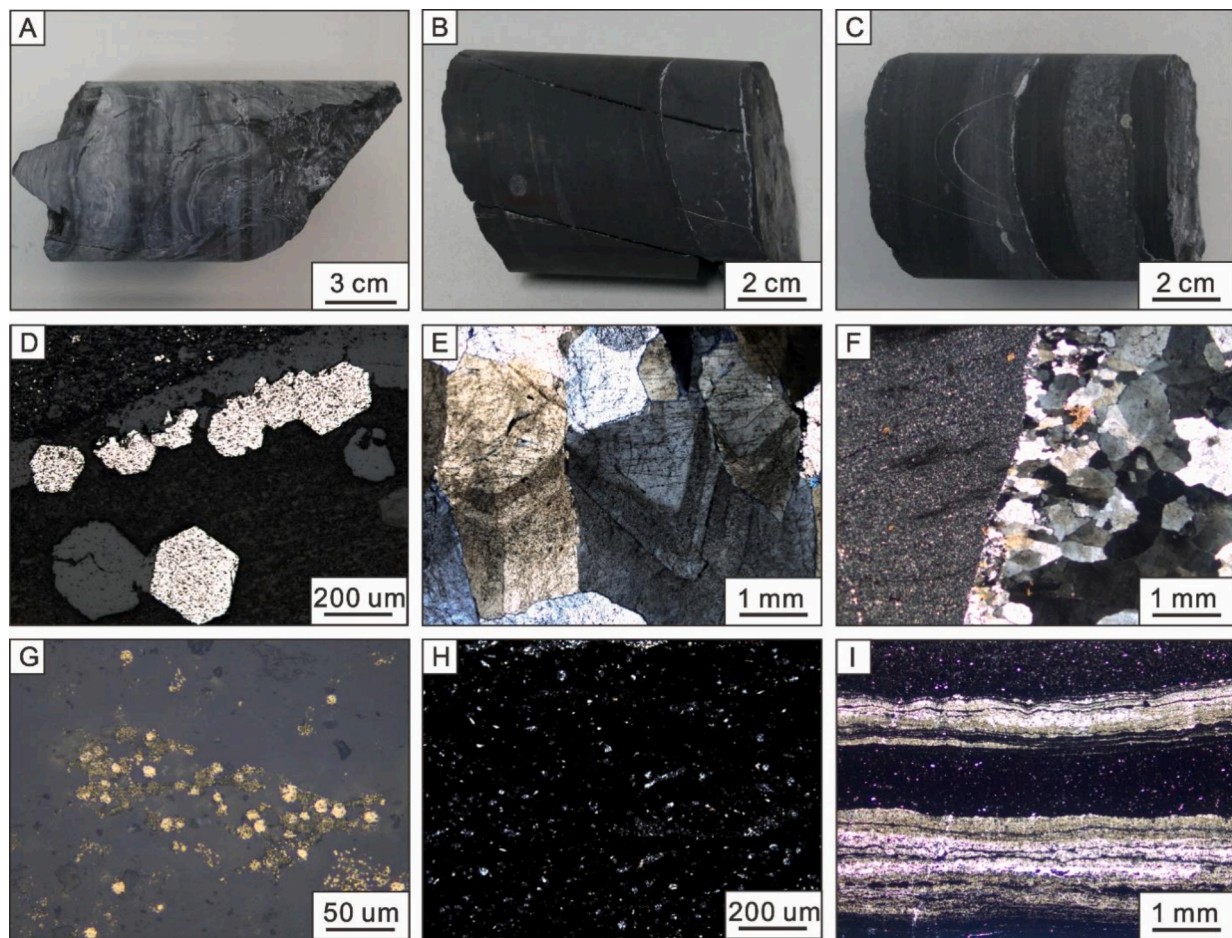


**Fig. 2.** Core and thin section images from the XAD1 well, illustrating the lithological and petrographic characteristics of the Liuchapo and Niutitang Formations. (A) Core photograph of a typical Liuchapo chert sample at 885.6 m. (B) Core photograph of Niutitang black shale at 869.2 m. (C) Core photograph of Niutitang siliceous shale at 867.7 m. (D) Thin section showing well-preserved microcrystalline quartz from the Liuchapo chert at 872 m. (E) Thin section highlighting coarse quartz crystals at 874 m. (F) Thin section displaying bedded microcrystalline quartz and organic matter (left) with hydrothermal coarse quartz throughout the sedimentary layers (right) of the Liuchapo chert at 885 m. (G) Thin section revealing framboidal textures in chert at the base of the Liuchapo Formation, at 902 m. (H) Thin section showing diffused organic matter and amorphous biogenic silica in the Niutitang black shale. (I) Thin section illustrating an interbedded structure of black shale and microcrystalline quartz in the Liuchapo siliceous shale lithofacies at 909 m.

**Table 1**

Major and trace element concentrations along with iron speciation indices of the XAD1 borehole samples.

Sample	Lithofacies	Depth (m)	TOC (%)	TS (%)	$^{13}\text{C}_{\text{org}}$ (‰)	Sc <sup>45</sup>	Mn <sup>55</sup>	Ba <sup>137</sup>	Th <sup>232</sup>	U <sup>238</sup>	Mo <sup>95</sup>	Al (%)	Ti (%)	Fe (%)	Fe <sub>HR</sub> /Fe <sub>T</sub>	Fe <sub>py</sub> /Fe <sub>HR</sub>
XAD-1	black shale	866	0.78	0.96	-31.47	5.38	169.02	2729.66	3.31	1.14	1.26	2.06	0.10	1.49	0.51	0.91
XAD-2	black shale	867	1.17	0.87	-30.81	3.55	180.31	2745.10	3.41	1.82	1.48	1.45	0.07	1.20	0.56	0.92
XAD-3	black shale	867.5	2.46	1.28	-31.17	7.37	795.81	2058.08	3.18	1.54	1.93	1.61	0.08	1.12	0.58	0.90
XAD-4	black shale	868	2.29	1.90	-31.74	5.90	920.19	1268.89	3.94	1.97	1.47	1.69	0.09	1.57	0.61	0.93
XAD-5	black shale	868.7	1.19	3.20	-31.12	7.95	153.20	2415.64	7.19	1.71	2.01	4.02	0.24	4.41	0.59	0.94
XAD-6	black shale	869.4	0.86	2.31	-31.24	5.02	166.69	1325.31	3.11	1.60	2.50	3.00	0.11	4.70	0.43	0.93
XAD-7	siliceous shale	870.2	0.92	4.96	-31.15	12.62	124.75	3146.33	12.55	2.57	2.04	6.74	0.41	7.05	0.37	0.94
XAD-8	black shale	871.5	0.69	2.98	-30.66	15.90	1603.99	1849.72	5.89	5.53	1.50	3.44	0.20	2.71	0.27	0.70
XAD-9	black shale	872	0.48	2.39	-29.16	36.71	455.24	2513.76	11.24	9.35	3.98	5.63	0.46	11.72	0.09	0.62
XAD-10	black shale	872.5	0.59	2.62	-30.03	17.08	1792.96	1035.08	4.04	2.79	1.27	2.66	0.17	2.30	0.26	0.64
XAD-11	Chert	873	0.35	0.07	-32.94	1.06	7.58	457.93	0.74	1.17	0.35	0.21	0.01	0.13	0.78	0.29
XAD-12	Chert	873.5	0.28	0.13	-32.8	1.40	4.61	1420.43	0.90	0.96	1.04	0.26	0.01	0.17	0.75	0.40
XAD-13	Chert	874	0.53	0.06	-32.95	0.85	8.79	472.77	0.24	0.28	0.90	0.13	0.00	0.05	0.74	0.20
XAD-14	Chert	874.5	0.64	0.71	-32.92	3.33	14.33	354.44	2.63	1.29	0.85	0.51	0.02	0.36	0.87	0.93
XAD-15	Chert	875	0.66	0.26	-32.8	3.20	320.48	320.46	0.74	1.26	0.75	0.52	0.02	0.66	0.38	0.70
XAD-16	Chert	875.3	0.53	0.19	-32.86	5.68	13.58	391.76	0.43	0.46	0.55	0.48	0.02	0.36	0.63	0.57
XAD-17	Chert	876.2	0.08	0.17	-33.26	2.38	201.40	274.94	0.49	0.31	0.30	0.35	0.01	0.25	0.64	0.59
XAD-18	Chert	876.8	0.29	0.23	-32.35	3.26	7.26	339.91	0.95	0.45	0.27	0.46	0.02	0.34	0.75	0.67
XAD-19	Chert	877.4	0.86	0.31	-33.16	3.71	31.48	356.10	0.88	0.55	0.45	0.48	0.02	0.40	0.70	0.63
XAD-20	Chert	878	1.27	0.52	-32.88	9.43	18.67	591.56	1.11	1.18	1.13	1.11	0.04	0.71	0.65	0.69
XAD-21	Chert	878.5	0.87	1.20	-33.02	5.71	3979.66	341.88	0.38	0.12	0.29	0.13	0.01	0.66	0.81	0.41
XAD-22	Chert	879	0.22	0.33	-32.48	7.91	44.15	422.42	0.78	0.63	0.69	0.70	0.02	0.48	0.47	0.64
XAD-23	Chert	879.5	0.65	0.49	-32.95	8.44	22.68	728.28	8.10	4.20	1.61	1.16	0.06	0.84	0.55	0.64
XAD-24	Chert	880	0.10	0.17	-33.16	2.32	9.62	353.07	0.97	0.58	0.42	0.45	0.02	0.29	0.91	0.38
XAD-25	Chert	880.5	0.13	0.09	-31.83	1.75	8.82	213.85	0.36	0.35	0.52	0.24	0.01	0.12	0.82	0.47
XAD-26	Chert	881.4	0.79	0.27	-32.63	7.78	8.81	453.53	0.86	0.91	0.81	0.76	0.02	0.37	0.66	0.66
XAD-27	Chert	881.8	0.60	0.20	-32.69	4.11	7.86	333.80	0.72	0.68	0.84	0.52	0.02	0.31	0.57	0.59
XAD-28	Chert	882.8	0.72	0.14	-32.93	5.52	6.39	421.66	1.13	1.76	0.79	0.52	0.02	0.25	0.76	0.55
XAD-29	Chert	883.3	0.57	0.11	-32.05	4.16	4.30	391.99	0.38	0.98	0.65	0.46	0.02	0.19	0.89	0.61
XAD-30	Chert	883.9	0.25	0.08	-31.06	1.47	5.68	215.70	0.49	0.80	0.39	0.17	0.01	0.14	0.60	0.58
XAD-31	Chert	884.2	0.47	0.09	-32.25	2.54	3.51	317.79	1.31	1.26	0.51	0.31	0.01	0.12	0.98	0.49
XAD-32	Chert	884.9	0.32	0.11	-32.83	2.33	6.01	448.77	0.65	1.23	0.97	0.48	0.02	0.16	0.62	0.43
XAD-33	Chert	885.3	0.53	0.17	-32.71	2.16	5.75	338.98	0.48	1.58	2.45	0.31	0.01	0.25	0.51	0.59
XAD-34	Chert	885.6	0.31	0.21	-32.24	1.56	6.61	247.06	0.47	1.64	0.93	0.20	0.01	0.42	0.38	0.76
XAD-35	Chert	886.4	0.23	0.08	-31.15	3.31	36.67	75.23	0.13	0.56	0.19	0.06	0.00	0.12	0.65	0.63
XAD-36	Chert	887.5	0.42	0.12	-32.06	0.91	3.73	71.51	0.14	0.46	0.29	0.07	0.00	0.16	0.75	0.84
XAD-37	Chert	887.8	0.15	0.07	-32.36	0.70	3.52	117.08	0.28	0.56	0.26	0.11	0.01	0.09	0.64	0.31
XAD-38	Chert	888.9	0.45	0.14	-32.95	3.75	13.25	414.88	0.68	2.80	1.56	0.44	0.01	0.19	0.79	0.62
XAD-39	Chert	889.3	0.48	0.12	-32.67	2.98	11.66	317.63	0.85	3.33	2.52	0.31	0.01	0.15	0.83	0.37
XAD-40	Chert	889.7	0.57	0.11	-32.29	1.39	34.15	134.00	0.36	1.89	0.71	0.10	0.00	0.16	0.76	0.61

(continued on next page)

**Table 1** (continued)

Sample	Lithofacies	Depth (m)	TOC (%)	TS (%)	$\delta^{13}\text{C}_{\text{org}}$ (‰)	$\text{Sc}^{45}$ (ppm)	$\text{Mn}^{55}$ (ppm)	$\text{Ba}^{137}$ (ppm)	$\text{Th}^{232}$ (ppm)	$\text{U}^{238}$ (ppm)	$\text{Mo}^{95}$ (ppm)	Al (%)	Ti (%)	Fe (%)	$\text{Fe}_{\text{HR}}/\text{Fe}_{\text{T}}$	$\text{Fe}_{\text{py}}/\text{Fe}_{\text{HR}}$
XAD-41	Chert	890	0.30	0.10	-32.64	2.79	23.41	248.87	0.64	3.54	1.62	0.22	0.01	0.15	0.54	0.65
XAD-42	Chert	890.6	0.43	0.11	-32.47	3.62	13.85	295.40	1.31	5.92	1.36	0.27	0.01	0.16	0.73	0.65
XAD-43	Chert	891.1	0.26	0.05	-32.7	2.36	37.59	193.34	0.70	3.35	1.19	0.17	0.01	0.22	0.25	0.35
XAD-44	Chert	891.8	0.59	0.07	-32.95	3.35	20.29	239.20	0.76	4.35	1.72	0.21	0.01	0.10	0.74	0.42
XAD-45	Chert	892	0.37	0.06	-32.51	1.66	18.30	186.96	0.17	0.94	0.61	0.14	0.00	0.07	0.86	0.49
XAD-46	Chert	893.6	0.33	0.04	-32.37	3.05	20.94	165.19	0.41	3.58	1.51	0.15	0.01	0.04	0.92	0.32
XAD-47	Chert	893.8	0.39	0.06	-32.09	3.14	93.01	81.52	0.22	0.59	0.79	0.09	0.00	0.06	0.62	0.49
XAD-48	Chert	894.1	0.40	0.04	-32.74	2.68	11.47	155.81	0.34	2.42	1.09	0.13	0.01	0.04	0.88	0.43
XAD-49	Chert	894.6	0.77	0.13	-33.16	0.00	0.01	0.17	0.00	0.00	0.00	0.24	0.02	0.14	0.81	0.66
XAD-50	Chert	866	0.69	0.08	-32.94	1.87	10.32	171.39	0.47	3.37	2.17	0.15	0.01	0.10	0.93	0.69
XAD-51	Chert	867	0.60	0.06	-32.65	1.18	8.48	144.33	0.21	1.24	0.82	0.11	0.01	0.05	0.77	0.30
XAD-52	Chert	867.5	0.64	0.06	-33.17	3.14	64.18	151.41	0.27	1.96	1.78	0.11	0.01	0.07	0.96	0.48
XAD-53	Chert	868	0.45	0.06	-33.22	2.07	59.80	166.71	0.38	4.55	1.57	0.14	0.01	0.06	0.69	0.34
XAD-54	Chert	868.7	0.88	0.04	-32.07	3.28	45.94	136.14	0.29	3.18	0.96	0.11	0.01	0.02	0.81	0.17
XAD-55	Chert	869.4	0.44	0.07	-32.39	2.28	8.81	238.76	0.67	9.30	4.22	0.21	0.01	0.09	0.71	0.63
XAD-56	Chert	870.2	0.68	0.14	-31.8	2.91	38.20	229.55	0.65	22.92	13.98	0.18	0.01	0.16	0.67	0.49
XAD-57	Chert	871.5	0.97	0.17	-33.42	5.02	90.08	239.45	0.76	24.09	18.66	0.20	0.01	0.18	0.81	0.51

dolomite, and pyrite (<10 %) (Table 1). The siliceous shales exhibit a composition similar to the black shales but with less quartz and slightly more clay (~2%) (Table 1).

#### 4.2. Organic C isotope and metal element proxies

The organic carbon isotope maintains stable values ( $\delta^{13}\text{C}_{\text{org}}$ : -32.61 ± 0.50 ‰) among the Liuchapo chert samples, while a notable positive excursion (~3‰) occurs at the onset of the Niutitang black shale ( $\delta^{13}\text{C}_{\text{org}}$ : -30.86 ± 0.76 ‰) (Fig. 3). TOC and TS are also low in Liuchapo samples (0.50 ± 0.25 wt%; 0.17 ± 0.20 wt%) and much higher in Niutitang samples (1.14 ± 0.69 wt%; 2.30 ± 1.20 wt%) (Fig. 3).

To ensure the effectiveness of the Fe speciation method, 15 samples very close to and above the  $\text{Fe}_{\text{T}}$  threshold ( $\text{Fe}_{\text{T}} > 0.5\%$ , all distributed in the upper 15 m of the intervals) were selected, although samples with lower  $\text{Fe}_{\text{T}}$  were also tested. The selected samples show  $\text{Fe}_{\text{HR}}/\text{Fe}_{\text{T}}$  ratios averaging 0.48 ± 0.19 and  $\text{Fe}_{\text{py}}/\text{Fe}_{\text{HR}}$  ratios averaging 0.77 ± 0.17 (Fig. 3), with both ratios showing low values at the Liuchapo-Niutitang boundary. Al and Mn are very low in the chert and then markedly elevated in the black shale (Table 2). Both  $\text{U}_{\text{EF}}^*$  (average 1.84 ± 1.44) and  $\text{Mo}_{\text{EF}}^*$  (average 2.66 ± 2.98) show shorter period variations throughout the study interval with peaks occurring in the base of the Liuchaopo chert and the Niutitang black shale.  $\text{Mo}_{\text{xs}}/\text{U}_{\text{xs}}$  (average 2.42 ± 2.45) ratios are generally below 1 throughout the Liuchaopo interval with some single high values, while having a high value in the middle part of the studied Niutitang shales (Fig. 3).

#### 4.3. REY distribution

In contrast to the Fe speciation, we also remove the REE concentration results for the Niutitang shale samples due to the complexity and multiplicity of REE signals in the mudstone when used to discuss the

redox condition of the water column (Zhang and Shields, 2022). The total REE concentrations ( $\Sigma\text{REE}$ ) of the Liuchapo cherts show a wide range from 1.25 ppm to 121.52 ppm with an average of 16.64 ppm, and most of the samples are significantly lower than the PAAS values (Fig. 4A; Table 2).  $\text{La}_{\text{n}}/\text{Yb}_{\text{n}}$  values are low (average  $0.26 \pm 0.24$ ) indicating strong HREE enrichment and no significant La (average  $0.88 \pm 0.28$ ) and Gd (average  $1.06 \pm 0.17$ ) anomalies were observed (Table 3).  $\text{Ce}_{\text{n}}/\text{Ce}_{\text{n}}^*$  ratios vary from 0.33 to 1.46 and most samples show moderate negative Ce anomalies (average  $0.70 \pm 0.25$ ), with a period variation throughout the chert interval (Fig. 3). All  $\text{Eu}_{\text{n}}/\text{Eu}_{\text{n}}^*$  ratios are positive except for sample XAD-43 ( $\text{Eu}_{\text{n}}/\text{Eu}_{\text{n}}^* = 0.97$ ) with some extreme peaks. Given that the high positive Eu anomalies may be an artificial result of ICP-MS testing due to the influence of barium compounds (e.g.,  $\text{BaO}^+$ ), we excluded chert samples that commonly have high Ba concentrations and extremely positive Eu anomalies. Additionally, the Eu values are presented after correcting for potential Ba interference using the relationship (Dulski, 1994; Wei et al., 2020):

$$\text{Eu}_{\text{cor}} = \text{Eu} - 0.00022 \times \text{Ba} \quad (6)$$

The Y concentration shows a marked enrichment in the lower part of the chert than in the upper part, as indicated by the elevated  $\text{Y}_{\text{n}}/\text{Y}_{\text{n}}^*$  and Y/Ho ratios (885–900 m, average  $1.69 \pm 0.15$  and  $41.81 \pm 3.41$ ; 873–885 m, average  $1.14 \pm 0.16$  and  $29.42 \pm 3.39$ ) (Table 3).

Based on sedimentological and geochemical proxy data, the XAD1 well section is divided into three distinct stages for the following discussion (Fig. 3): Stage I (885–900 m, with an equivalent Ediacaran age): Dominated by Liuchapo chert, characterized by bedded cherts with high quartz content and minor organic matter. Stage II (873–885 m, with an equivalent age roughly ranges from terminal Ediacaran to terminal Cambrian Stage 2): Also composed of Liuchapo chert, but potentially showing transitional features in mineral composition and sedimentary

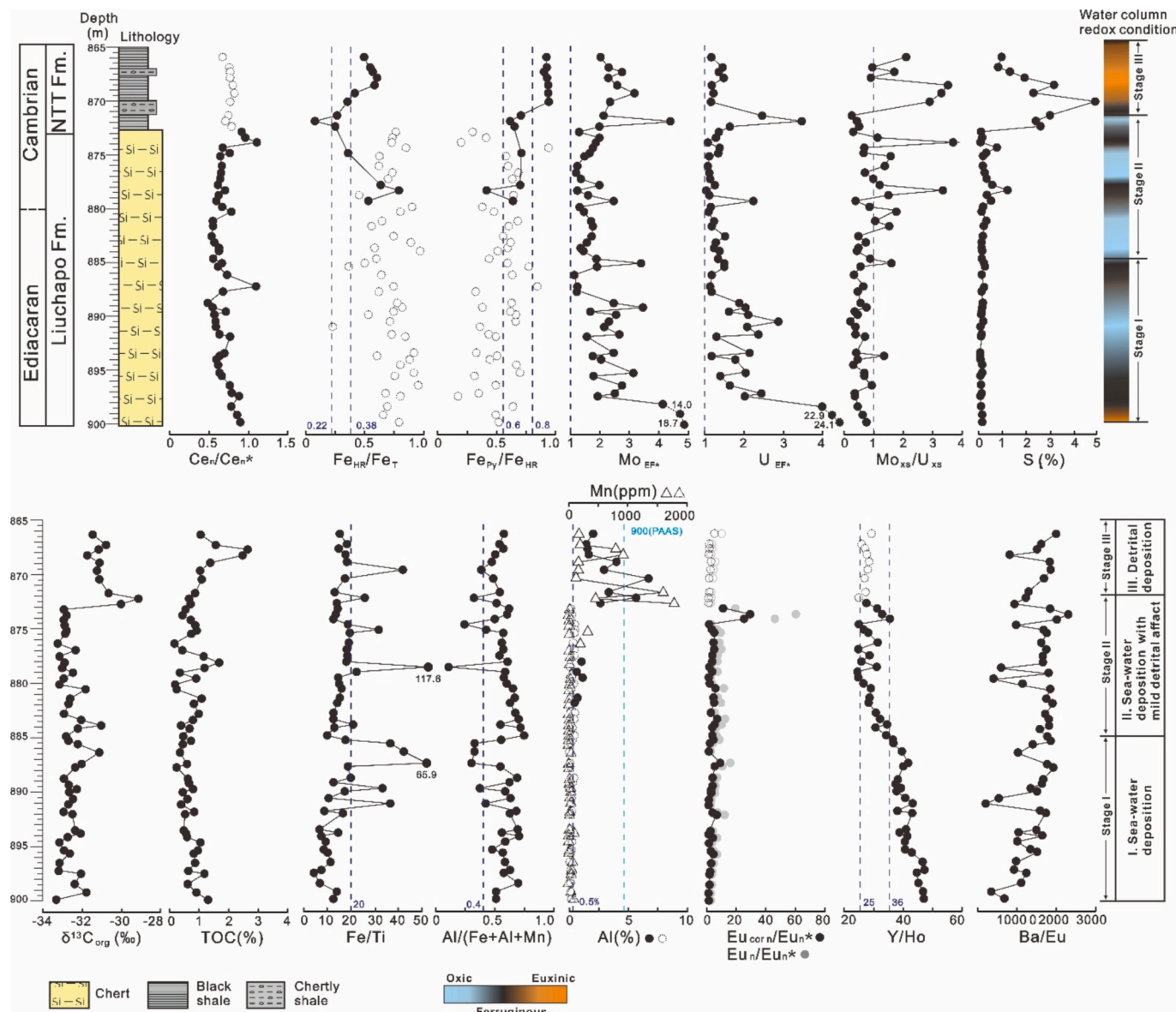


**Fig. 3.** Geochemical data for the studied XAD1 borehole from the Liuchapo chert and Niuitang mudstone formations. Dashed hollow circles in the  $\text{Fe}_{\text{HR}}/\text{Fe}_T$  and  $\text{Fe}_{\text{py}}/\text{Fe}_{\text{HR}}$  plots represent unreliable Fe speciation values for Liuchapo chert samples, where total Fe concentrations are significantly lower than 0.5 %. Dashed hollow circles in the REE plot ( $\text{Ce}_n/\text{Ce}_n^*$ ,  $\text{Eu}_n/\text{Eu}_n^*$ ) also indicate geochemical signals excluded from the Niuitang black shale Formation. Similarly, dashed hollow circles in the Al plot denote samples with Al concentrations below 0.5 wt%.  $\text{Eu}_{\text{corr}}$  = corrected Eu anomalies based on Ba concentrations.

geochemistry signals. Stage III (865–873 m, with an equivalent age roughly ranges from terminal Cambrian Stage 2 to Cambrian Stage 3): Marked by the Niuitang black shale, characterized by high organic matter content and a significant presence of detrital and biogenic silica.

## 5. Discussion

### 5.1. Direct hydrothermal contribution to Liuchapo chert

Seawater, which is the largest reservoir of dissolved silica on Earth's surface, estimated at approximately 240 Tmol, ultimately receives its silica from both continental weathering and hydrothermal activity (Tréguer et al., 2021). Terrestrial influence of chert deposition can be inferred from Al content, with values above 0.5 % indicating detrital input, while Ti content serves as an additional indicator of terrestrial material input (Delvigne et al., 2012). In Liuchapo samples, Al content remains well below the PAAS average, except for a few samples in Stage II where values approach or slightly exceed the 0.5 wt% threshold

(Fig. 3). Ti content in all chert samples ( $0.01 \pm 0.01$  %) is also an order of magnitude lower than PAAS ( $\text{Ti}_{\text{PAAS}} = 0.60$  %, Table 1), suggesting minimal detrital influence during deposition that similar with the typical hydrothermally influenced Proterozoic chert formation (Jasper) in central Arizona, USA (Slack et al., 2007). These results indicate that the silica in the Liuchapo chert is predominantly of marine authigenic origin.

Modern seawater typically displays depletion of light REE and large positive Y anomalies (Fig. 4B), with values between 40 and 80 in open marine environments and lower values (33–40) in nearshore or restricted settings (Bau et al., 1997; De Baar et al., 1985; Nozaki et al., 1997). Y/Ho ratios greater than 40 in Precambrian cherts and over 36 in carbonates are considered as the reliable indicators of seawater signatures, while lower values suggest terrestrial input (Delvigne et al., 2012; Tostevin et al., 2016). In Stage I of our samples, Y/Ho ratios are consistently high, all exceeding 36, and show no correlation with Al content (Fig. 5H). In contrast, Stage II displays a marked decrease in Y/Ho ratios, although most values remain above 25, and a weak

**Table 2**

Rare Earth Element (REE) indices of the XAD1 borehole samples.

Sample	Depth (m)	La <sup>139</sup>	Ce <sup>140</sup>	Pr <sup>141</sup>	Nd <sup>146</sup>	Sm <sup>147</sup>	Eu <sup>153</sup>	Gd <sup>157</sup>	Tb <sup>159</sup>	Dy <sup>163</sup>	Y <sup>89</sup>	Ho <sup>165</sup>	Er <sup>166</sup>	Tm <sup>169</sup>	Yb <sup>172</sup>	Lu <sup>175</sup>
		(ppm)	(ppm)	(ppm)	(ppm)	(ppm)	(ppm)	(ppm)								
XAD-1	866	8.32	12.89	1.64	4.92	0.69	1.38	0.75	0.13	0.82	5.58	0.19	0.65	0.12	0.72	0.11
XAD-2	867	5.58	12.26	2.27	11.08	3.44	1.71	2.52	0.44	2.15	9.53	0.37	0.90	0.12	0.66	0.09
XAD-3	867.5	9.21	17.27	2.45	9.32	2.41	1.37	1.98	0.38	2.24	12.32	0.46	1.30	0.21	1.29	0.19
XAD-4	868	6.41	13.79	2.60	13.06	4.49	1.55	3.67	0.68	3.58	18.20	0.65	1.60	0.22	1.25	0.19
XAD-5	868.7	13.41	21.40	2.45	7.90	1.25	1.31	1.26	0.22	1.32	9.17	0.32	1.13	0.22	1.39	0.23
XAD-6	869.4	10.69	16.40	1.83	5.84	0.87	0.72	0.85	0.14	0.86	5.42	0.19	0.63	0.12	0.72	0.11
XAD-7	870.2	35.40	59.84	7.77	26.99	3.09	1.86	2.78	0.44	2.41	15.49	0.58	2.11	0.41	2.44	0.40
XAD-8	871.5	16.57	26.84	3.93	14.87	3.68	1.42	2.98	0.56	3.02	16.62	0.61	1.81	0.31	1.87	0.31
XAD-9	872	58.05	86.19	12.35	42.97	6.26	2.05	5.25	0.86	4.40	24.72	0.99	3.28	0.61	3.75	0.66
XAD-10	872.5	14.76	23.76	3.47	13.87	3.80	1.10	2.98	0.58	3.17	17.47	0.64	1.85	0.33	1.98	0.34
XAD-11	873	0.24	0.38	0.05	0.21	0.06	0.25	0.06	0.01	0.09	0.71	0.02	0.08	0.01	0.08	0.02
XAD-12	873.5	0.27	0.44	0.05	0.21	0.05	0.62	0.06	0.01	0.08	0.56	0.02	0.06	0.01	0.08	0.01
XAD-13	874	0.12	0.18	0.02	0.10	0.03	0.24	0.02	0.00	0.04	0.37	0.01	0.04	0.01	0.06	0.01
XAD-14	874.5	1.52	3.19	0.66	3.20	1.09	0.36	0.88	0.15	0.86	4.23	0.17	0.47	0.08	0.47	0.08
XAD-15	875	1.55	2.51	0.33	1.15	0.17	0.19	0.16	0.02	0.14	0.90	0.03	0.13	0.03	0.19	0.03
XAD-16	875.3	1.76	2.95	0.40	1.21	0.14	0.22	0.16	0.02	0.11	0.75	0.03	0.11	0.02	0.16	0.03
XAD-17	876.2	0.73	1.20	0.18	0.60	0.11	0.17	0.12	0.02	0.13	0.88	0.03	0.10	0.02	0.12	0.02
XAD-18	876.8	1.80	2.82	0.37	1.13	0.12	0.20	0.13	0.01	0.09	0.60	0.02	0.09	0.02	0.13	0.02
XAD-19	877.4	1.69	2.69	0.39	1.26	0.18	0.22	0.19	0.03	0.18	1.25	0.04	0.16	0.03	0.22	0.04
XAD-20	878	3.67	5.97	0.83	2.48	0.30	0.36	0.33	0.04	0.24	1.64	0.06	0.24	0.05	0.38	0.07
XAD-21	878.5	1.46	3.03	0.60	2.94	1.19	0.57	1.25	0.23	1.23	7.10	0.23	0.62	0.10	0.62	0.11
XAD-22	879	2.25	3.63	0.54	1.74	0.19	0.23	0.22	0.03	0.21	1.33	0.05	0.21	0.04	0.29	0.06
XAD-23	879.5	5.89	13.38	3.46	18.54	7.33	1.79	6.05	0.96	5.15	22.67	0.91	2.39	0.35	2.15	0.37
XAD-24	880	1.05	1.97	0.40	1.88	0.61	0.31	0.56	0.07	0.44	2.21	0.08	0.24	0.04	0.24	0.04
XAD-25	880.5	0.19	0.28	0.04	0.18	0.05	0.12	0.08	0.01	0.12	0.82	0.03	0.10	0.02	0.13	0.02
XAD-26	881.4	2.02	3.21	0.51	1.53	0.18	0.26	0.22	0.03	0.27	2.12	0.07	0.29	0.06	0.41	0.08
XAD-27	881.8	1.80	2.40	0.33	0.89	0.09	0.18	0.13	0.02	0.18	1.44	0.05	0.20	0.04	0.27	0.05
XAD-28	882.8	3.20	4.94	0.78	2.27	0.25	0.25	0.32	0.05	0.43	3.69	0.12	0.47	0.09	0.69	0.12
XAD-29	883.3	1.09	1.58	0.23	0.65	0.09	0.22	0.11	0.02	0.13	1.12	0.03	0.15	0.03	0.20	0.04
XAD-30	883.9	0.41	0.64	0.09	0.30	0.06	0.12	0.06	0.01	0.14	1.20	0.03	0.14	0.02	0.18	0.03
XAD-31	884.2	0.53	0.89	0.16	0.65	0.16	0.20	0.16	0.03	0.23	1.72	0.06	0.19	0.03	0.23	0.04
XAD-32	884.9	3.97	5.31	0.73	1.94	0.20	0.25	0.27	0.04	0.25	2.27	0.07	0.24	0.05	0.32	0.06
XAD-33	885.3	0.61	0.86	0.13	0.48	0.10	0.18	0.13	0.03	0.25	2.49	0.07	0.26	0.05	0.37	0.07
XAD-34	885.6	0.41	0.70	0.15	0.70	0.23	0.18	0.27	0.06	0.44	3.97	0.11	0.36	0.07	0.45	0.08
XAD-35	886.4	0.19	0.31	0.05	0.25	0.11	0.07	0.24	0.10	0.91	9.91	0.25	0.84	0.15	0.96	0.17
XAD-36	887.5	0.03	0.06	0.01	0.04	0.01	0.04	0.02	0.01	0.08	0.91	0.02	0.09	0.02	0.14	0.02
XAD-37	887.8	0.21	0.29	0.04	0.15	0.03	0.06	0.04	0.01	0.08	0.75	0.02	0.07	0.01	0.09	0.01
XAD-38	888.9	2.57	3.48	0.55	1.43	0.15	0.25	0.25	0.05	0.44	4.52	0.12	0.44	0.09	0.63	0.12
XAD-39	889.3	1.51	2.15	0.33	0.93	0.13	0.20	0.21	0.05	0.41	4.51	0.12	0.46	0.10	0.67	0.12
XAD-40	889.7	0.20	0.31	0.05	0.22	0.07	0.10	0.13	0.04	0.43	4.85	0.12	0.46	0.09	0.63	0.11
XAD-41	890	1.11	1.49	0.23	0.67	0.13	0.17	0.21	0.06	0.60	6.59	0.17	0.62	0.13	0.81	0.14
XAD-42	890.6	3.72	6.47	1.52	7.20	2.14	0.54	2.23	0.43	2.80	25.36	0.62	1.86	0.32	1.87	0.31
XAD-43	891.1	7.88	14.45	3.28	15.28	4.38	0.94	4.69	0.90	5.67	54.95	1.26	3.63	0.58	3.16	0.48
XAD-44	891.8	0.59	0.80	0.11	0.35	0.07	0.15	0.16	0.05	0.57	6.51	0.17	0.63	0.13	0.85	0.16
XAD-45	892	0.12	0.18	0.03	0.11	0.04	0.11	0.06	0.01	0.13	1.40	0.03	0.12	0.02	0.15	0.02
XAD-46	893.6	0.48	0.76	0.11	0.40	0.10	0.11	0.18	0.06	0.64	7.84	0.19	0.70	0.14	0.93	0.17
XAD-47	893.8	0.47	0.78	0.14	0.57	0.15	0.08	0.22	0.05	0.36	2.91	0.07	0.23	0.04	0.23	0.04
XAD-48	894.1	0.56	0.77	0.11	0.34	0.05	0.10	0.09	0.03	0.28	3.49	0.08	0.31	0.06	0.41	0.08
XAD-49	894.6	/	/	/	/	/	/	/	/	/	/	/	/	/	/	/
XAD-50	895.4	0.77	1.19	0.18	0.59	0.11	0.13	0.18	0.05	0.49	6.27	0.15	0.56	0.11	0.75	0.12
XAD-51	895.6	0.54	0.78	0.11	0.38	0.06	0.10	0.09	0.02	0.19	2.31	0.05	0.20	0.04	0.28	0.05
XAD-52	896.5	0.91	1.51	0.21	0.81	0.17	0.16	0.24	0.05	0.41	4.65	0.10	0.35	0.06	0.39	0.06
XAD-53	897.3	0.98	1.60	0.21	0.76	0.20	0.18	0.33	0.09	0.81	10.77	0.23	0.84	0.15	0.98	0.16
XAD-54	897.6	0.43	0.68	0.10	0.43	0.14	0.11	0.23	0.06	0.55	6.61	0.15	0.52	0.10	0.63	0.10
XAD-55	898.5	3.20	5.61	0.75	2.77	0.45	0.22	0.52	0.11	0.74	8.87	0.19	0.73	0.13	0.89	0.16
XAD-56	899.3	5.93	13.28	2.10	9.88	2.49	0.66	2.79	0.52	3.21	35.29	0.75	2.22	0.34	1.91	0.30
XAD-57	900	2.51	5.54	0.81	3.76	0.97	0.35	1.11	0.22	1.57	19.73	0.41	1.39	0.25	1.55	0.26

**Table 3**

X-ray Diffraction (XRD) indices of the XAD1 borehole samples.

Sample	Depth (m)	Quartz (%)	K-feldspar (%)	Calcite (%)	Dolomite (%)	Pyrite (%)	Clay minerals (%)
Xrd-1	868	63.4	0.0	0.0	0.0	4.4	32.2
Xrd-2	869	58.6	4.4	3.3	7.1	6.2	20.4
Xrd-3	871	84.3	4.3	5.4	/	4.0	2.0
Xrd-4	875	85.0	/	5.9	8.6	/	0.5
Xrd-5	882	92.4	2.6	5.0	/	/	/
Xrd-6	893	99.5	/	0.2	0.3	/	/
Xrd-7	897	84.3	4.3	5.4		4.0	2.0

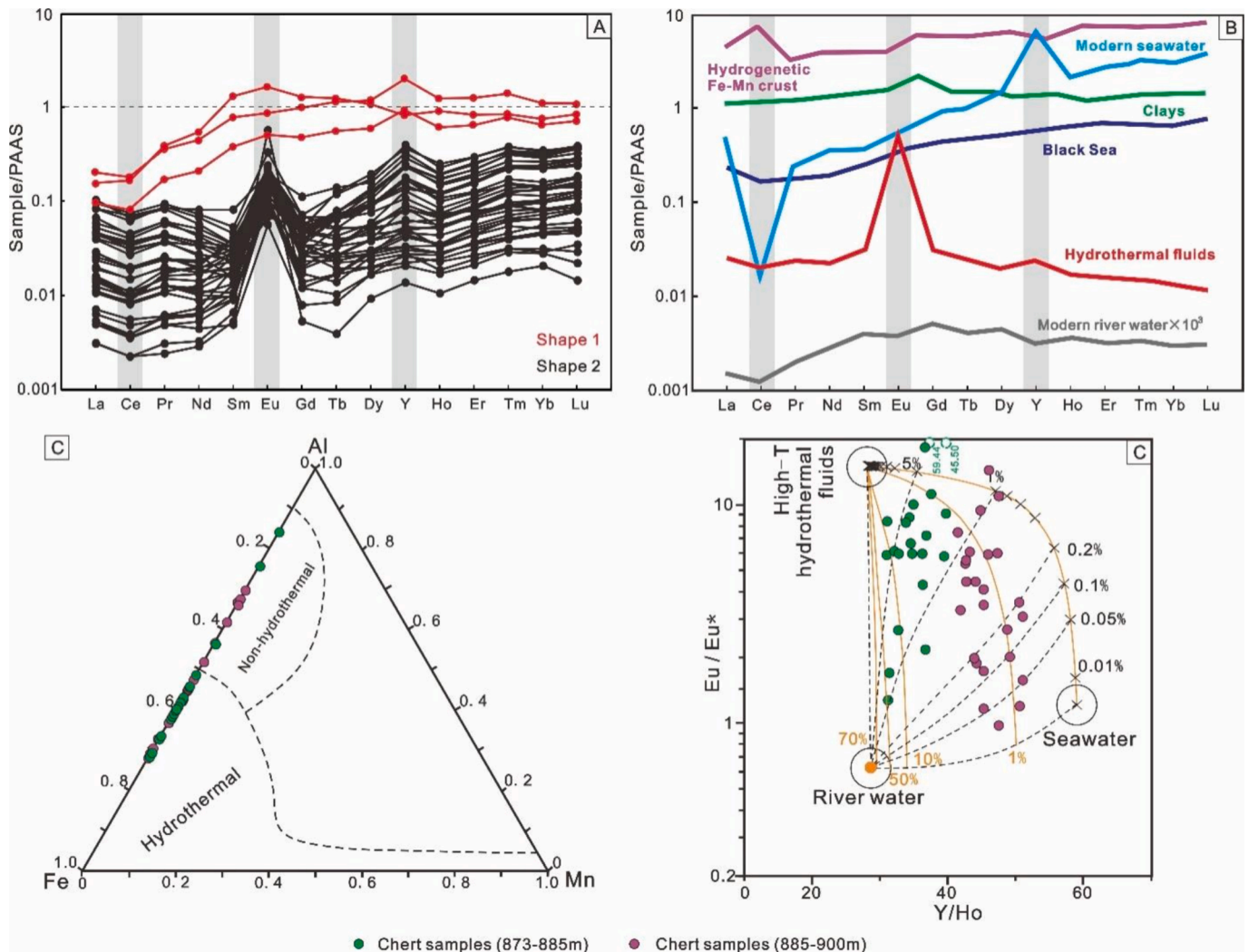


**Fig. 4.** PAAS-normalized REE distributions for Liuchapo chert samples from the XAD1 borehole. (A) Two distinct shapes of PAAS-normalized REE and Y (REY) distribution diagrams for Liuchapo chert samples, based on Taylor and McLennan (1985). (B) REY distribution patterns representing key natural environments and minerals, showing typical anomalies such as Ce, Eu, and Y. Data sources for the REY include marine hydrogenic Fe-Mn crusts and high-temperature hydrothermal (black-smoker) fluids from Bau and Dulski (1996), modern seawater from James et al. 1995, riverine water from Soyol-Erdene and Huh (2013), and authigenic carbonates and clays from Tostevin et al. (2016). Silicon discrimination for the Liuchapo cherts. (C) Fe-Al-Mn (wt%) ternary diagram for chert genesis, based on Adachi et al. (1986). (D) Cross-plot of Y/Ho ratios and Eu anomalies (Eu<sub>n</sub> / Eu<sub>n</sub> \*) in the Liuchapo cherts, where the three end-members represent modern high-temperature hydrothermal fluids (Bau and Dulski, 1999), modern seawater (Alibo and Nozaki, 1999), and modern river water (Soyol-Erdene and Huh, 2013).

correlation with Al content (Fig. 5H). These patterns further indicate a limited detrital influence on the chert deposition, particularly in Stage I.

For marine authigenic siliceous formations, the Al-Fe-Mn ternary diagram is a widely used tool to differentiate the origins of siliceous rocks (Adachi et al., 1986; Yamamoto, 1987). This diagram is based on Cretaceous cherts and porcellanite samples formed in hydrothermal environments on or near active ridges. Basal hydrothermal deposits with low Al/(Al + Fe + Mn) ratios reflect rapid volcanic spreading rates, while basal metalliferous sediments exhibit higher Al/(Al + Fe + Mn) ratios compared to sediments from typical oceanic ridges (Adachi et al., 1986; Yamamoto, 1987). Thus, the hydrothermal siliceous rocks are characterized by low Al/(Al + Fe + Mn) ratios (<0.4; Murray, 1994) and high Fe/Ti ratios (>20; Boström, 1983), distinguishing them from siliceous rocks with more substantial detrital input. Here, several chert samples show contemporaneously low Al/(Al + Fe + Mn) ratios and high Fe/Ti values (Fig. 3), suggesting that this layer was influenced by periodic hydrothermal silicon input. Additionally, in the Al-Fe-Mn ternary diagram for siliceous rock genesis (Fig. 4C), the data points are scattered across both hydrothermal and non-hydrothermal regions, indicating a substantial marine silicon and iron flux. The cross plot of

Eu<sub>n</sub>/Eu<sub>n</sub>\* versus Y/Ho shows a notable upward shift, particularly for the upper Liuchapo samples from 873 to 885 m (Fig. 4D). This implies that a portion of the silica may have originated from direct precipitation via seafloor hydrothermal fluids. Also, the petrographic analysis shows bedded microcrystalline quartz with occasional macrocrystalline and coarse quartz crystals throughout the sedimentary layers (Fig. 2D, E, F), suggesting episodic input of higher-temperature fluids, which is consistent with a periodic hydrothermal contribution.

The REE distributions exhibit a low concentration of LREE along with distinctive geochemical anomalies: a notable negative Ce anomaly, a positive Y anomaly, and a pronounced positive Eu anomaly (Fig. 4A, B). These patterns suggest a mixed source, incorporating modern seawater deposition as well as hydrothermal fluid influence. Excess Eu relative to neighboring mid-REE (MREE) in marine sediments often indicates the influence of high-temperature hydrothermal fluids from mid-ocean ridge-type systems on the dissolved REE load of seawater (Derry and Jacobsen, 1990; Bau and Dulski, 1999). However, caution must be exercised, particularly for samples with high Ba/Eu ratios (e.g., Ba/Eu > 10,000, Zepeda et al., 2024), as during ICP-MS analysis, a fraction of Ba is oxidized to BaO<sup>+</sup> in the plasma (Shibata et al., 1993). This leads to

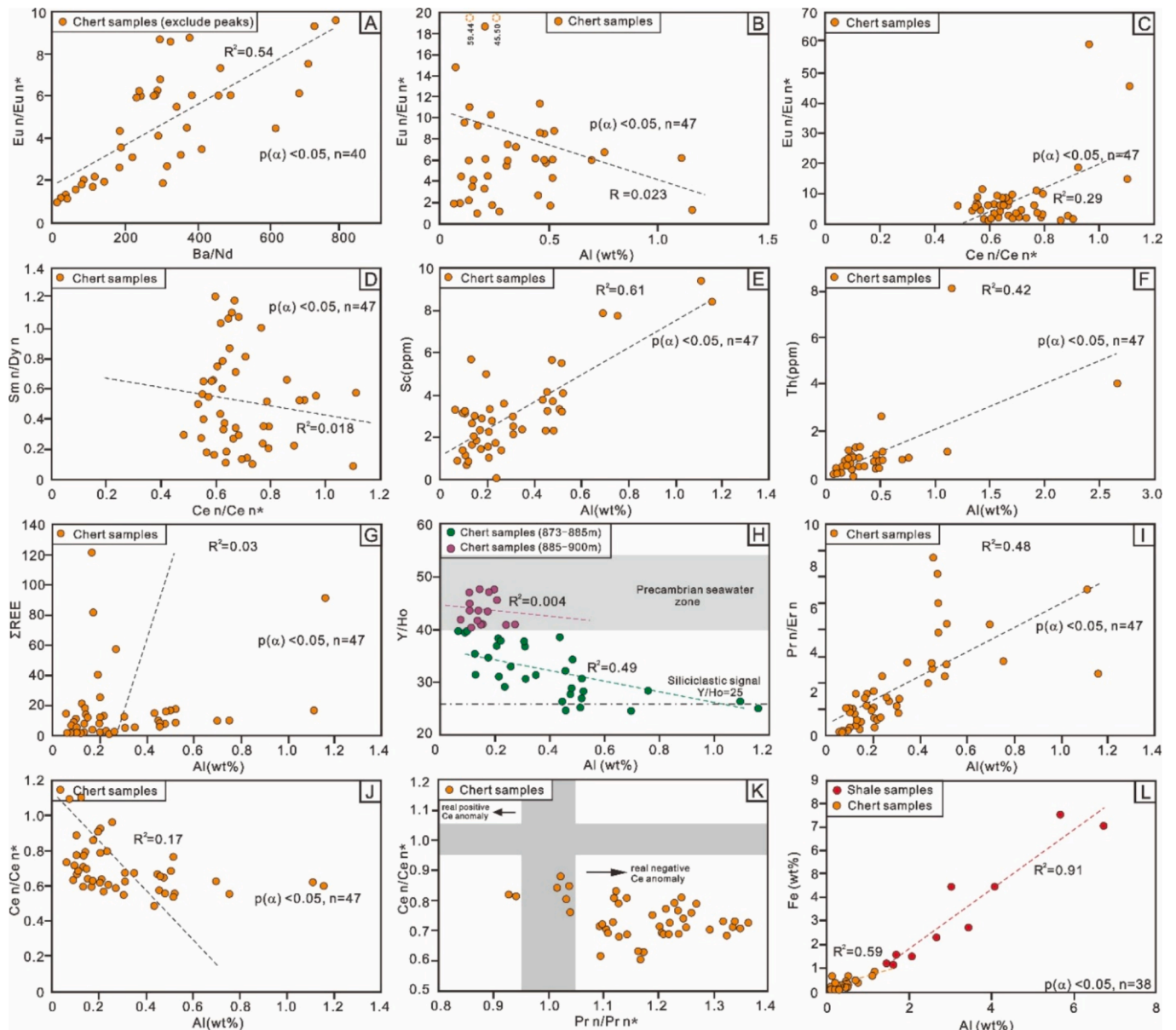


**Fig. 5.** Cross plots for assessing the effectiveness of geochemical proxies in the Liuchapo cherts and Niutitang Formation: (A) A broad positive correlation between Eu/Eu<sub>n\*</sub> and Ba/Nd suggests a possible ICP-MS testing effect on Eu anomalies in samples with high Ba concentrations; (C-D) Lack of correlation between Ce<sub>n</sub>/Ce<sub>n\*</sub> with Eu<sub>n</sub>/Eu<sub>n\*</sub> and Sm<sub>n</sub>/Dy<sub>n</sub> implies minimal diagenetic alteration; (B, E-J) Relationships between Al and Eu<sub>n</sub>/Eu<sub>n\*</sub>, Al-Sc, Al-Th, Al-ΣREE (the sum of REEs), Al-Y/Ho, Al-Pr<sub>n</sub>/Er<sub>n</sub> (the fractionation between light REE and heavy REE), and Al-Ce<sub>n</sub>/Ce<sub>n\*</sub> in the Liuchapo chert. Elements such as Al, Sc, and Th serve as indicators of detrital input. The lack of correlations between Al and Eu<sub>n</sub>/Eu<sub>n\*</sub>, Al and ΣREE, Al and Y/Ho (especially in the 873–885 m interval), Al and Pr<sub>n</sub>/Er<sub>n</sub>, or Al and Ce<sub>n</sub>/Ce<sub>n\*</sub> indicates minimal terrigenous contamination affecting the REE distribution. (K) Using the arithmetic calculation for Pr<sub>n</sub>/Pr<sub>n\*</sub> (Pr<sub>n</sub>/(0.5Ce<sub>n</sub> + 0.5Nd<sub>n</sub>)) versus Ce<sub>n</sub>/Ce<sub>n\*</sub> (Ce<sub>n</sub>/(0.5La<sub>n</sub> + 0.5Pr<sub>n</sub>)) discrimination plot (Bau and Dulski, 1996), La and Ce anomalies are distinguished by this plot. (L) High Fe and Al concentrations and their strong correlation in Niutitang samples confirm a detrital Fe source.

isobaric interferences on both Eu isotopes ( $^{135}\text{Ba}^{16}\text{O}^+$  on  $^{151}\text{Eu}^+$  and  $^{137}\text{Ba}^{16}\text{O}^+$  on  $^{153}\text{Eu}^+$ ), potentially resulting in inaccurate or uncertain Eu abundance estimates (Barrat et al., 2020; Zepeda et al., 2024). Although our chert samples do not have such high Ba/Eu ratios over 10,000 (Fig. 3, Zepeda et al., 2024), the Eu anomalies, without peak values exceeding 10 (40 in 47), still show small correlation with Ba/Nd (Fig. 5A), suggesting a potential degree of ICP-MS testing effect. To minimize experimental error, we calculated and corrected the Eu anomaly using the formula presented in Equation (6). Although the corrected Eu anomaly (Eu<sub>cor n</sub>/Eu<sub>n\*</sub>) was significantly reduced especially for extreme values, the chert samples still show a clear Eu anomaly after correction ( $4.63 \pm 5.29$ , Fig. 3). This indicates that despite potential testing errors, the Liuchapo chert retains distinct geochemical

characteristics of hydrothermal precipitation.

Additionally, plagioclase minerals in terrigenous debris can exhibit positive Eu anomalies due to fractional crystallization, but the lack of correlation between Eu anomalies and Al concentrations in our samples largely rules out detrital interference (Fig. 5B). No notable biological structures were identified in our samples (Fig. 2), indicating a possible inorganic chert origin. Thus, based on our lithofacies and high-resolution geochemical evidence, hydrothermal processes played a crucial role in the formation of the Liuchapo chert in the XAD1 area. Submarine hydrothermal fluids may have mixed with ocean waters either in the early stages or from more distant sources, enriching seawater with silica and leading to the precipitation of supersaturated silicon, consistent with previous studies (Dong et al., 2015; Li et al.,

2022). Also, the direct precipitation of hydrothermal fluids may have significantly contributed to chert formation in our samples. Hydrothermal activity may have been more frequent than previously recognized, influencing a larger and potentially shallower area, periodically impacting the outer slope where the XAD1 well is located.

### 5.2. Redox dynamics on the outer slope near E-C boundary

Diagenetic alteration and contamination from non-chemical deposition (e.g., REEs in clay minerals) should be considered when interpreting REE data (Shields and Stille, 2001; Nothdurft et al., 2004; Zhang et al., 2018). However, REEs in chert or carbonate are generally resistant to post-depositional diagenesis (Zhang and Shields, 2022), and most samples in our study show minimal diagenetic recrystallization, as evidenced by petrographic features observed under optical microscopy (Fig. 2). Additionally, negative correlations between  $\text{Ce}_n/\text{Ce}_n^*$  and  $\text{Eu}_n/\text{Eu}_n^*$  or  $\text{Dy}_n/\text{Sm}_n$ , which often indicate diagenetic alteration (Shields and Stille, 2001), were not observed in the studied succession (Fig. 5C, D), suggesting that our Ce anomalies remained largely unaffected by diagenesis. Furthermore, as discussed in section 5.1, no clear covariation was observed between aluminum (Al), scandium (Sc), or thorium (Th) (used as indicators of detrital input) and various REE parameters (e.g., ΣREE, Y/Ho ratios, LREE/HREE fractionation ( $\text{Pr}_n/\text{Er}_n$ ), or Ce anomalies, Fig. 5E-J). These findings strongly support the preservation and extraction of primary seawater REE signals in our chert samples. Most of our negative Ce anomaly signals are reliable due to high  $\text{Pr}_n/\text{Pr}_n^*$  values (>1.05), though samples with lower  $\text{Pr}_n/\text{Pr}_n^*$  may be slightly affected by elevated La concentrations (Fig. 5K). Additionally, the significantly elevated Fe and Al content, along with their strong correlation (Fig. 5L), suggest a predominantly detrital source for Fe, ensuring the reliability of Fe speciation in assessing redox conditions for the shale samples.

Our approach clearly demonstrates that the XAD1 data reflect changes in the intensity of reducing conditions, with intervals of fluctuating (sub)oxic conditions occurring over short timescales, particularly in the Liuchapo Formation (as identified by fluctuating but ubiquitous Ce anomalies, Fig. 3, Stage I-II). These intervals were separated by phases where the water column was likely dominated by ferruginous to euxinic conditions, particularly in the lowermost Liuchapo and the main Niutitang formations (Fig. 3), indicating a highly oscillating water column chemocline. While evidence from the contemporaneous Dengying Formation suggests significant marine oxygenation on carbonate platforms (Ling et al., 2013), interpreting deep-water oxygenation at the slope setting requires caution. The strong negative Ce anomalies in the Liuchapo cherts might also result from siliceous phytoplankton in the photic zone above the chemocline (Braun and Chen, 2003; Guo et al., 2007). However, the absence of well-preserved biological structures in our samples points to predominantly inorganic, hydrothermal processes for chert formation. Thus, the Ce anomalies and trace elements at XAD1 likely reflect the most oxygenated conditions situation that experienced in this slope environment.

The predominantly euxinic intervals (stage III) in the Niutitang shale coincide with consistent enrichments in  $\text{Fe}_{\text{py}}/\text{Fe}_{\text{HR}}$  and  $\text{Mo}_{\text{xs}}/\text{U}_{\text{xs}}$  ratios, indicative of euxinia (Fig. 3). The increase in TOC content and the pronounced positive  $\delta^{13}\text{C}_{\text{org}}$  excursion at the Liuchapo-Niutitang boundary (Fig. 3) are mirrored in both shallower slope environments (Wu et al., 2022) and across the widespread carbonate platform in South China, where the Liuchapo chert transitions to the isochronous Dengying carbonate formation (Goldberg et al., 2007; Li et al., 2013; Cremonese et al., 2013; Chen et al., 2015). Coupled with the significant rise in TS and multiple S isotopic compositions of pyrite ( $\delta^{34}\text{S}_{\text{py}}$  and  $\delta^{33}\text{S}_{\text{py}}$ ) (Li et al., 2020), demonstrating an expansive increase in organic matter and pyrite burial throughout the Yangtze-Nanhua Basin, likely driven by the proliferation of euxinic conditions (Yang et al., 2022). Thus, combining our high-resolution geochemical data, the gradual oxygenation trend observed in the outer slope environment of the XAD1 region from the late Ediacaran gave way to a rapid, downward expansion of a

euxinic wedge during the early Cambrian.

The initial driver of the oceanic redox shift close to ECB may have stemmed from intensified continental weathering and increased clay input, as indicated by Li (Wei et al., 2024) and Sr isotope evidence (Bataille et al., 2017). This surge in weathering likely introduced a substantial influx of bio-limiting nutrients, elevating marine primary productivity to near-modern levels (Liu et al., 2024). This productivity boost is evidenced by modern seawater-like Cd isotope values observed in the uppermost Liuchapo chert Formation (Liu et al., 2024) and widespread negative nitrogen isotope excursions across sections of varying depths (Cremonese et al., 2013; Kikumoto et al., 2014; Wang et al., 2015; Wu et al., 2022) (Fig. 6). Although spatial and temporal variations in nitrogen cycling may reflect the enhanced biological nitrogen fixation linked to biotic evolution (Chen et al., 2019), multiple nutrient proxies point to a significant increase in marine primary productivity, by fueling the sinking and subsequent decomposition of organic matter during the earliest Cambrian, directly triggering marine deoxygenation.

### 5.3. Controls on the termination of chert system

The cessation of chert deposition was governed by a combination of terrigenous inputs and marine geochemical changes. The “Great Unconformity,” a globally recognized sedimentary gap between the Cambrian and Ediacaran strata, likely driven by tectonic shifts, marks a pronounced global sea-level fall (Sun et al., 2023; Bowyer et al., 2024). While deep-water deposition in South China during this interval has generally been considered continuous (Xue and Zhou, 2006), an increase in Al concentrations observed in the earliest Niutitang Formation samples suggests a sharp rise in detrital inputs. This influx, coupled with an oxic-to-suboxic transition (as indicated by Mn enrichment, Fig. 3), signals a redox shift from the anoxic conditions of the uppermost Liuchapo Formation. The change in slope depositional settings, corresponding with a hiatus in shallow-water environments at the Ediacaran-Cambrian boundary, may be linked to the global sea-level drop. The continued influx of detrital material accelerated sedimentation, rendering the environment unsuitable for the slow deposition of siliceous rocks. Later, a widespread and pronounced transgression dominated the Nanhua Basin in the early Cambrian (Peng et al., 2020), leading to the deposition of Niutitang organic-rich mudstones.

Although the XAD1 samples reveal a hydrothermal contribution to the formation of the Liuchapo chert, such signatures are not widespread across the entire Nanhua Basin. Hydrothermal inputs may locally enhance silicon concentrations in seawater; however, studies of other Ediacaran-Cambrian boundary (ECB) cherts, including those from South China, Tarim, and Oman (Ramseyer et al., 2013; Yu et al., 2009), show REE distributions characteristic of seawater, with minimal Eu anomalies and notably low Ge/Si ratios (0.2–0.5  $\mu\text{mol/mol}$ ; Li et al., 2022). These values are an order of magnitude lower than those of hydrothermal fluids (8–14  $\mu\text{mol/mol}$ ; Evans and Derry, 2002), suggesting that continental weathering fluxes still likely served as the primary source of silicon to contemporaneous seawater in these regions (Froelich et al., 1992; Chang et al., 2009; Li et al., 2022). With abundant dissolved silica from both continental and hydrothermal sources, the deposition of the Liuchapo chert likely occurred through a cyclic process of co-precipitation and dissolution involving Fe oxyhydroxide and silicic acid, driven by oscillating chemocline shifts in the water column (Reddy et al., 2016; Zheng et al., 2016). In seawater, Fe(III)-Si gels formed when Fe oxyhydroxides co-precipitated with silicic acid. Around the redox boundary, Fe(III) was reduced to  $\text{Fe}^{2+}$ , releasing it from the gels, while amorphous silica precipitated through  $\text{Si(OH)}_4$  polymerization near or below the sediment–water interface (SWI), depositing the silica (Fischer and Knoll, 2006). Here,  $\text{Fe}^{2+}$  was recycled as a shuttle, facilitating continued Si deposition and the formation of bedded cherts (Fig. 7A; Li et al., 2022). However, near the Liuchapo-Niutitang boundary, this Fe-Si loop likely weakened as marine deoxygenation pushed the chemocline

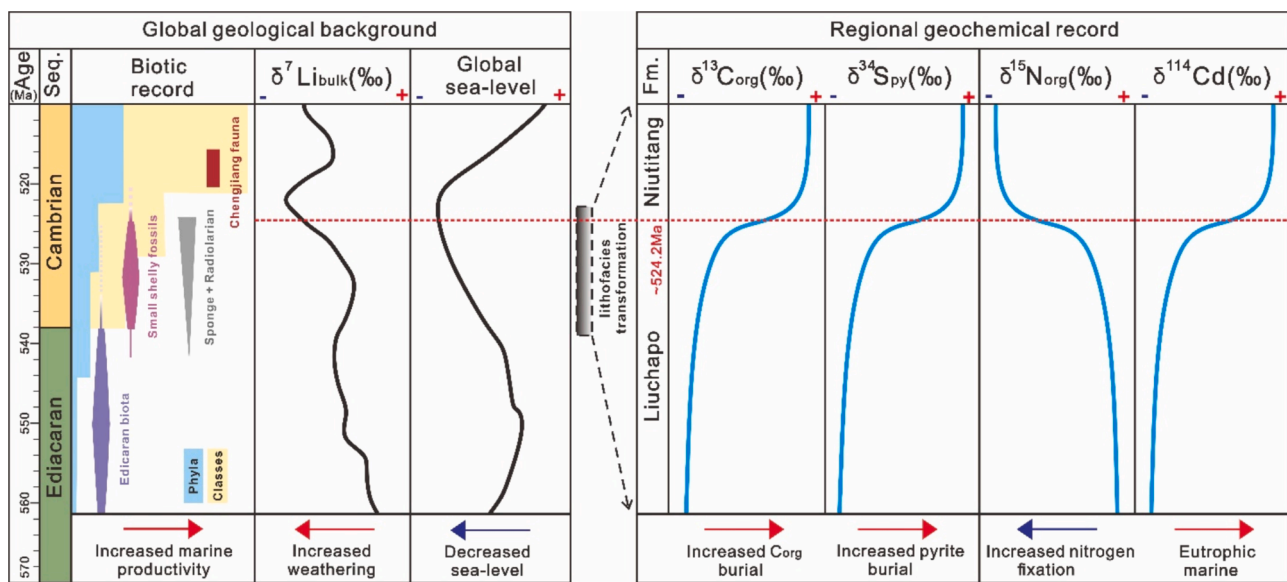


**Fig. 6.** Biostratigraphic and chemostratigraphic changes through the Late Ediacaran to Early Cambrian period. The figure summarizes the important fossil records (Zhu et al., 2017; Zhang et al., 2021a,b; Ye et al., 2021) and global phyla and class diversity variations (Erwin et al., 2011). Data of mudstone  $\delta^7\text{Li}$  (Wei et al., 2024) and global sea-level changes (Van der Meer et al., 2017) are listed as the long-term geological background throughout the ECT. Regional redox evolution, nutrient dynamics, and key isotope records across the Liuchapo chert to Niutitang black shale boundary are presented, including generalized  $\delta^{13}\text{C}_{\text{org}}$  (Guo et al., 2013; Wu et al., 2022, and this study),  $\delta^{34}\text{S}_{\text{py}}$  (Li et al., 2020),  $\delta^{15}\text{N}$  (Cremonese et al., 2013; Wu et al., 2022), and  $\delta^{114}\text{Cd}$  (Liu et al., 2024). Abbreviations: Org = organic matter; py = pyrite.

into shallower depths, limiting Fe (III) reduction above the SWI and hindering  $\text{Si(OH)}_4$  transport. The expansion of euxinic conditions from the shelf to the slope replaced the previously oscillating oxic to ferruginous conditions, leading to the trapping of dissolved  $\text{Fe}^{2+}$  as pyrite burial. This process inhibited Fe oxidation and disrupted chert deposition (Fig. 7B). As a result, the weakened Fe-Si cycle likely reduced further chert formation at the Liuchapo–Niutitang boundary.

Regardless of the specific geochemical mechanisms for silicon deposition, the Ediacaran ocean was characterized by high concentrations of dissolved silicon due to the absence of biogenic uptake, with silicon precipitating inorganically once it reached saturation with amorphous silica or other silicate phases (e.g., Siever, 1992; Ison and Planavsky, 2018). Fossil evidence suggests that the evolution of silica-secreting organisms, particularly sponges and radiolarians, saw significant development during the Ediacaran-Cambrian transition (ca. 551–523 Ma), especially in South China (Ye et al., 2021; Zhang et al., 2021a,b; Fig. 6). Silica precipitation on organic matter likely occurs due to abiotic interactions between exposed organic functional groups and dissolved silica in seawater, forming structures like Althel silicilite (Stolper et al., 2017). This type of silica precipitation may have been significantly enhanced by elevated primary productivity and the widespread anoxic conditions that characterized the Liuchapo deposition at the Ediacaran-Cambrian transition (Escario et al., 2020; Chang et al., 2020, Fig. 6). Additionally, Si isotope data and mass-balance models from the Liuchapo chert indicate that the radiation of these siliceous organisms led to an approximately 80 % decline in oceanic dissolved Si concentrations (Ye et al., 2021). This transition fundamentally shifted the ocean from a Precambrian state, saturated with respect to inorganic Si-bearing phases, to a Phanerozoic state below saturation (Maliva et al., 1989; Conley et al., 2017). As silicon availability declined, the deposition of chert ceased, allowing organisms to redirect energy to other metabolic processes, fostering greater ecological diversification and leading to the replacement of dominant Ediacaran molluscs by small shell-bearing fauna, as evidenced by the biotic record showing a transition from Ediacaran Biota to small shelly fossils (Fig. 6) (Knoll, 2003; Erwin et al., 2011; Zhu et al., 2017). This shift may have played a crucial role in paving the way for the Cambrian Explosion.

## 6. Conclusions

This study provides a comprehensive analysis of the controls on the deposition and termination of the massive Liuchapo chert system during the Ediacaran-Cambrian transition (ECT) in the Nanhua Basin, South China. By integrating high-resolution geochemical proxies, including Fe speciation, rare earth elements plus yttrium (REE + Y) systematics, and redox-sensitive trace metals, we uncover the interplay between hydrothermal activity, redox dynamics, and silica cycling in shaping this significant lithofacies transition.

Our results demonstrate that the Liuchapo chert was predominantly formed through marine authigenic processes with episodic hydrothermal contributions, as evidenced by low Al and Ti contents, high Fe/Ti ratios, and positive Eu anomalies. Fluctuating oxic to ferruginous conditions characterized the redox environment of the Liuchapo Formation, transitioning to persistent euxinic conditions in the overlying Niutitang Formation. This transition disrupted the Fe-Si loop critical for chert deposition, marking a pivotal shift in the marine silica cycle. Increased terrigenous input, driven by intensified continental weathering during the ECT, likely contributed additional nutrients to the marine system, enhancing productivity and accelerating deoxygenation in slope settings.

The emergence and proliferation of silica-secreting organisms during the ECT played a significant role in depleting dissolved silica levels in the ocean. This ecological shift heralded the transformation from Precambrian oceans saturated with respect to inorganic silica phases to Phanerozoic oceans undersaturated with silica, fundamentally altering marine biogeochemical cycles. The abrupt cessation of chert deposition, coupled with the rapid expansion of euxinic conditions, reflects a major reorganization of oceanic environments during this critical interval. This study underscores the importance of combining sedimentological, geochemical, and paleoenvironmental data to understand the complex processes governing lithofacies transitions during key geological periods. By shedding light on the mechanisms driving the termination of the Liuchapo chert system, our findings contribute to a deeper understanding of the dynamic environmental and ecological changes that set the stage for the Cambrian Explosion.

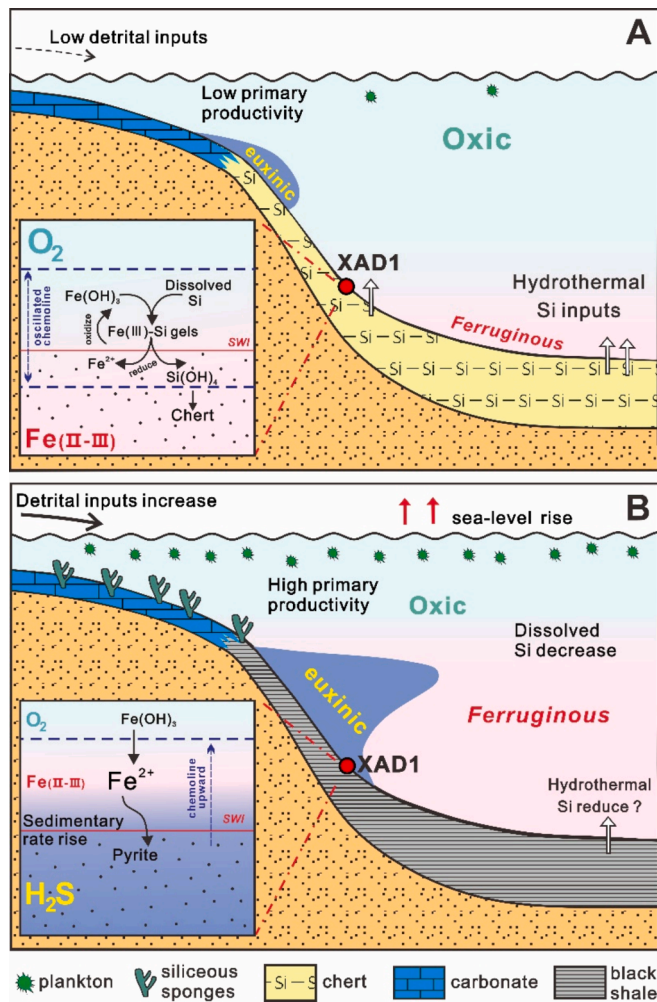


**Fig. 7.** Schematic diagram illustrating the mechanisms controlling Liuchapo chert formation (A) and cessation (B). The diagram captures key geochemical and environmental processes during the late Ediacaran to early Cambrian period, including silica supply from both hydrothermal and continental weathering sources, Fe-Si cycling near the redox boundary, and the role of euxinia in halting chert deposition. The decline of dissolved silicon in the oceans due to the rise of silica-secreting organisms and marine deoxygenation is also highlighted, showing the transition from extensive chert formation to the widespread deposition of the Niutitang black shales.

#### CRediT authorship contribution statement

**Yuxuan Wang:** Writing – review & editing, Writing – original draft, Methodology, Investigation, Data curation, Conceptualization. **Fang Hao:** Supervision, Funding acquisition. **Yangbo Lu:** Writing – review & editing, Visualization, Data curation. **Kaixun Zhang:** Resources. **Yan Ye:** Methodology, Data curation. **Shang Xu:** Project administration, Funding acquisition, Data curation.

#### Declaration of competing interest

The authors declare that they have no known competing financial interests or personal relationships that could have appeared to influence the work reported in this paper.

#### Acknowledgements

This study was supported by the National Natural Science Foundation of China (Grant No. 42122017, Grant No. 41821002, and Grant No. 42472201) “CUG Scholar” Scientific Research Funds at China University

of Geosciences (Wuhan) (Project No. 2023099). We sincerely thank Dr. Kun Zhang from University College London, UK and Dr. Yijun Xiong from University of Leeds, UK for their valuable discussions and insights.

#### Data availability

I have shared all of my data in the manuscript.

#### References

- Adachi, M., Yamamoto, K., Sugisaki, R., 1986. Hydrothermal chert and associated siliceous rocks from the northern Pacific: their geological significance as indication old ocean ridge activity. *Sed. Geol.* 47, 125–148.
- Alcott, L.J., Krause, A.J., Hammarlund, E.U., Bjerrum, C.J., Scholz, F., Xiong, Y., Hobson, A.J., Neve, L., Mills, B.J.W., März, C., Schnetger, B., Bekker, A., Poulton, S. W., 2020. Development of Iron Speciation Reference Materials for Palaeoredox Analysis. *Geostand. Geoanal. Res.* 44, 581–591.
- Algeo, T.J., Li, C., 2020. Redox classification and calibration of redox thresholds in sedimentary systems. *Geochim. Cosmochim. Acta.* 287, 8–26.
- Alibo, D.S., Nozaki, Y., 1999. Rare earth elements in seawater: particle association, shale-normalization, and Ce oxidation. *Geochim. Cosmochim. Acta.* 63, 363–372.
- Anderson, R., Lefhuray, A., Fleisher, M., Murray, J., 1989. Uranium deposition in saanich inlet sediments, vancouver island. *Geochim. Cosmochim. Acta.* 53, 2205–2213.
- Anderson, T.F., Raiswell, R., 2004. Sources and mechanisms for the enrichment of highly reactive iron in euxinic Black Sea sediments. *Am. J. Sci.* 304, 203–233.
- Baronas, J.J., Hammond, D.E., McManus, J., Wheat, C.G., Siebert, C., 2017. A global Ge isotope budget. *Geochim. Cosmochim. Acta.* 203, 265–283.
- Barrat, J.-A., Bayon, G., Wang, X., Le Goff, S., Rouget, M.-L., Gueguen, B., Salem, D.B., 2020. A new chemical separation procedure for the determination of rare earth elements and yttrium abundances in carbonates by ICP-MS. *Talanta* 219, 121244.
- Bataille, C.P., Willis, A., Yang, X., Liu, X.-M., 2017. Continental igneous rock composition: A major control of past global chemical weathering. *Sci. Adv.* 3, e1602183.
- Bau, M., 1991. Rare-earth element mobility during hydrothermal and metamorphic fluid-rock interaction and the significance of the oxidation state of europium. *Chem. Geol.* 93, 219–230.
- Bau, M., Dulski, P., 1996. Distribution of yttrium and rare-earth elements in the Penge and Kuruman iron-formations, Transvaal Supergroup, South Africa. *Precambrian Res.* 79, 37–55.
- Bau, M., Dulski, P., 1999. Comparing yttrium and rare earths in hydrothermal fluids from the Mid-Atlantic Ridge: implications for Y and REE behaviour during near-vent mixing and for the Y/Ho ratio of Proterozoic seawater. *Chem. Geol.* 155, 77–90.
- Bau, M., Koschinsky, A., 2009. Oxidative scavenging of cerium on hydrous Fe oxide: evidence from the distribution of rare earth elements and yttrium between Fe oxides and Mn oxides in hydrogenetic ferromanganese crusts. *Geochim. J.* 43, 37–47.
- Bau, M., Möller, P., Dulski, P., 1997. Yttrium and lanthanides in eastern Mediterranean seawater and their fractionation during redox-cycling. *Mar. Chem.* 56, 123–131.
- Bekker, A., Planavsky, N., Rasmussen, B., Krapez, B., Hofmann, A., Slack, J., Rouxel, O., Konhauser, K., 2014. Iron formations: Their origins and implications for ancient seawater chemistry. *Treatise on Geochemistry*. Elsevier 561–628.
- Benkovitz, A., Matthews, A., Teutsch, N., Poulton, S.W., Bar-Matthews, M., Almogi-Labin, A., 2020. Tracing water column euxinia in Eastern Mediterranean Sapropels S5 and S7. *Chem. Geol.* 545, 119627.
- Böström, K., 1983. Genesis of ferromanganese deposits-diagnostic criteria for recent and old deposits, *Hydrothermal processes at seafloor spreading centers*. Springer 473–489.
- Bowyer, F.T., Wood, R.A., Yilales, M., 2024. Sea level controls on Ediacaran-Cambrian animal radiations. *Sci. Adv.* 10, ead06462.
- Braun, A., Chen, J., 2003. Plankton from Early Cambrian black shale series on the Yangtze Platform, and its influences on lithologies. *Prog. Nat. Sci.* 13, 777–782.
- Calvert, S., Pedersen, T., 1993. Geochemistry of recent oxic and anoxic marine sediments: implications for the geological record. *Mar. Geol.* 113, 67–88.
- Canfield, D.E., Raiswell, R., Westrich, J.T., Reaves, C.M., Berner, R.A., 1986. The use of chromium reduction in the analysis of reduced inorganic sulfur in sediments and shales. *Chem. Geol.* 54, 149–155.
- Chang, H., Chu, X., Feng, L., Huang, J., 2009. Terminal Ediacaran anoxia in deep-ocean: Trace element evidence from cherts of the Liuchapo Formation, South China. *Sci. China. Ser. d: Earth Sci.* 52, 807–822.
- Chang, S., Zhang, L., Clausen, S., Feng, Q., 2020. Source of silica and silicification of the lowermost Cambrian Yanjiahe Formation in the Three Gorges area. *Palaeogeogr., Palaeoclimatol., Palaeoecol.*, South China, p. 548.
- Charvet, J., 2013. The neoproterozoic-early Paleozoic tectonic evolution of the south china block: an overview. *J. Asian Earth Sci.* 74, 198–209.
- Chen, Y., Diamond, C.W., Stueken, E.E., Cai, C.F., Gill, B.C., Zhang, F.F., Bates, S.M., Chu, X.L., Ding, Y., Lyons, T.W., 2019. Coupled evolution of nitrogen cycling and redoxcline dynamics on the Yangtze Block across the Ediacaran-Cambrian transition. *Geochi. Cosochi. Acta.* 257, 243–265.
- Chen, D., Zhou, X., Fu, Y., Wang, J., Yan, D., 2015. New U-Pb zircon ages of the Ediacaran-Cambrian boundary strata in South China. *Terra Nova* 27, 62–68.
- Clarkson, M.O., Poulton, S.W., Guibaud, R., Wood, R.A., 2014. Assessing the utility of Fe/Al and Fe-speciation to record water column redox conditions in carbonate-rich sediments. *Chem. Geol.* 382, 111–122.

- Conley, D.J., Frings, P.J., Fontorbe, G., Clymans, W., Stadmark, J., Hendry, K.R., Marron, A.O., De La Rocha, C.L., 2017. Biosilicification drives a decline of dissolved Si in the oceans through geologic time. *Front. Mar. Sci.* 4, 397.
- Cremonese, L., Shields-Zhou, G., Struck, U., Ling, H.-F., Och, L., Chen, X., Li, D., 2013. Marine biogeochemical cycling during the early Cambrian constrained by a nitrogen and organic carbon isotope study of the Xiaotan section. South China. *Precambrian Res.* 225, 148–165.
- De Baar, H.J., Bacon, M.P., Brewer, P.G., Bruland, K.W., 1985. Rare earth elements in the Pacific and Atlantic Oceans. *Geochim. Cosmochim. Acta.* 49, 1943–1959.
- Delvigne, C., Cardinal, D., Hofmann, A., André, L., 2012. Stratigraphic changes of Ge/Si, REE+ Y and silicon isotopes as insights into the deposition of a Mesarchaeean banded iron formation. *Earth Planet. Sci. Lett.* 355, 109–118.
- Derry, L.A., Jacobsen, S.B., 1990. The chemical evolution of Precambrian seawater: evidence from REEs in banded iron formations. *Geochim. Cosmochim. Acta.* 54, 2965–2977.
- Dong, L., Shen, B., Lee, C.-T.-A., Shu, X.J., Peng, Y., Sun, Y., Tang, Z., Rong, H., Lang, X., Ma, H., Yang, F., Guo, W., 2015. Germanium/silicon of the Ediacaran-Cambrian Laobao cherts: Implications for the bedded chert formation and paleoenvironment interpretations. *Geochim. Geophys. Geosyst.* 16, 751–763.
- Dulski, P., 1994. Interferences of oxide, hydroxide and chloride analyte species in the determination of rare earth elements in geological samples by inductively coupled plasma-mass spectrometry. *Fresenius' J. Anal. Chem.* 350, 194–203.
- Erwin, D.H., Lafleur, M., Tweedt, S.M., Sperling, E.A., Pisani, D., Peterson, K.J., 2011. The Cambrian conundrum: early divergence and later ecological success in the early history of animals. *Science* 334, 1091–1097.
- Escarce, S., Nightingale, M., Humez, P., Tutolo, B.M., 2020. The contribution of aqueous catechol-silica complexes to silicification during carbonate diagenesis. *Geochim. Cosmochim. Acta.* 280, 185–201.
- Evans, M.J., Derry, L.A., 2002. Quartz control of high germanium/silicon ratios in geothermal waters. *Geology* 30, 1019–1022.
- Fischer, W.W., Knoll, A.H., 2006. An iron shuttle for deepwater silica in Late Archean and early Paleoproterozoic iron formation. *Soc. Am. Bull. preprint, Geol.*
- Froelich, P., Blanc, V., Mortlock, R., Chlirud, S., Dunstan, W., Udomkit, A., Peng, T.H., 1992. River fluxes of dissolved silica to the ocean were higher during glacials: Ge/Si in diatoms, rivers, and oceans. *Paleoceanography* 7, 739–767.
- German, C.R., Elderfield, H., 1990. Application of the Ce anomaly as a paleoredox indicator: the ground rules. *Paleoceanography* 5, 823–833.
- German, C.R., Holliday, B.P., Elderfield, H., 1991. Redox cycling of rare earth elements in the suboxic zone of the Black Sea. *Geochim. Cosmochim. Acta.* 55, 3553–3558.
- Goldberg, T., Strauss, H., Guo, Q., Liu, C., 2007. Reconstructing marine redox conditions for the Early Cambrian Yangtze Platform: evidence from biogenic sulphur and organic carbon isotopes. *Palaeogeogr., Palaeoclimatol., Palaeoecol.* 254, 175–193.
- Guo, Q., Shields, G.A., Liu, C., Strauss, H., Zhu, M., Pi, D., Goldberg, T., Yang, X., 2007. Trace element chemostratigraphy of two Ediacaran–Cambrian successions in South China: Implications for organosedimentary metal enrichment and silicification in the Early Cambrian. *Palaeogeogr., Palaeoclimatol., Palaeoecol.* 254, 194–216.
- Guo, Q., Strauss, H., Zhu, M., Zhang, J., Yang, X., Lu, M., Zhao, F., 2013. High resolution organic carbon isotope stratigraphy from a slope to basinal setting on the Yangtze Platform, South China: Implications for the Ediacaran–Cambrian transition. *Precambrian Res.* 225, 209–217.
- He, T., Ling, H., Chen, Y., Li, D., Yang, A., Wang, D., Wu, H., 2013. Geochemical characteristics and origin of Ediacaran Piyuan chert in the Lantian section, Xiuning, southern Anhui Province. *Geol. J. China Univ.* 19, 620–633.
- Helz, G., Miller, C., Charnock, J., Mosselmans, J., Patrick, R., Garner, C., Vaughan, D., 1996. Mechanism of molybdenum removal from the sea and its concentration in black shales: EXAFS evidence. *Geochim. Cosmochim. Acta.* 60, 3631–3642.
- Hughes, N.C., Peng, S., Bhargava, O.N., Ahluwalia, A.D., Walia, S., Myrow, P.M., Parcha, S.K., 2005. Cambrian biostratigraphy of the Tal Group, Lesser Himalaya, India, and early Tsanglangpuan (late early Cambrian) trilobites from the Nigali Dhar syncline. *Geol. Mag.* 142, 57–80.
- Isson, T.T., Planavsky, N.J., 2018. Reverse weathering as a long-term stabilizer of marine pH and planetary climate. *Nature* 560, 471–475.
- James, R., Elderfield, H., Palmer, M., 1995. The chemistry of hydrothermal fluids from the Broken Spur site, 29°N Mid-Atlantic Ridge. *Geochim. Cosmochim. Acta.* 59, 651–659.
- Kikumoto, R., Tahata, M., Nishizawa, M., Sawaki, Y., Maruyama, S., Shu, D., Han, J., Komiya, T., Takai, K., Ueno, Y., 2014. Nitrogen isotope chemostratigraphy of the Ediacaran and Early Cambrian platform sequence at Three Gorges, South China. *Gondwana Res.* 25, 1057–1069.
- Knoll, A.H., 2003. Biomineralization and evolutionary history. *Rev. Mineral. Geochem.* 54, 329–356.
- Kremer, C., Poulton, S.W., Newton, R.J., März, C., Mills, B.J.W., Wagner, T., 2024. Controls on the Termination of Cretaceous Oceanic Anoxic Event 2 in the Tarfaya Basin. *Morocco. Am. J. Sci.*, p. 324.
- Lawrence, M.G., Kamber, B.S., 2006. The behaviour of the rare earth elements during estuarine mixing—revisited. *Mar. Chem.* 100, 147–161.
- Li, C., Dong, L., Ma, H., Liu, H., Li, C., Pei, H., Shen, B., 2022. Formation of the massive bedded chert and coupled Silicon and Iron cycles during the Ediacaran–Cambrian transition. *Earth Planet. Sci. Lett.* p. 594.
- Li, D., Ling, H.-F., Shields-Zhou, G.A., Chen, X., Cremonese, L., Och, L., Thirlwall, M., Manning, C.J., 2013. Carbon and strontium isotope evolution of seawater across the Ediacaran–Cambrian transition: Evidence from the Xiaotan section, NE Yunnan, South China. *Precambrian Res.* 225, 128–147.
- Li, D., Zhang, X., Hu, D., Li, D., Zhang, G., Zhang, X., Ling, H.-F., Xu, Y., Shen, Y., 2020. Multiple S-isotopic constraints on paleo-redox and sulfate concentrations across the Ediacaran–Cambrian transition in South China. *Precambrian Res.* 349.
- Ling, H.-F., Chen, X., Li, D., Wang, D., Shields-Zhou, G.A., Zhu, M., 2013. Cerium anomaly variations in Ediacaran–earliest Cambrian carbonates from the Yangtze Gorges area, South China: Implications for oxygenation of coeval shallow seawater. *Precambrian Res.* 225, 110–127.
- Liu, Z., Dickson, A.J., Sun, H., Wu, Y., Qiu, Z., Tian, H., 2024. Cadmium isotope evidence for near-modern bio-productivity in the early Cambrian ocean. *Chem. Geol.* p. 663.
- Liu, P., Yin, C., Chen, S., Tang, F., Gao, L., 2013. The biostratigraphic succession of acanthomorphic acritarchs of the Ediacaran Doushantuo Formation in the Yangtze Gorges area, South China and its biostratigraphic correlation with Australia. *Precambrian Res.* 225, 29–43.
- Maliva, R.G., Knoll, A.H., Siever, R., 1989. Secular change in chert distribution: a reflection of evolving biological participation in the silica cycle. *Palaeos* 519–532.
- März, C., Poulton, S.W., Beckmann, B., Küster, K., Wagner, T., Kasten, S., 2008. Redox sensitivity of P cycling during marine black shale formation: Dynamics of sulfidic and anoxic, non-sulfidic bottom waters. *Geochim. Cosmochim. Acta.* 72, 3703–3717.
- McLennan, S.M., 2001. Relationships between the trace element composition of sedimentary rocks and upper continental crust. *Geochim. Geophys. Geosyst.* 2, 1021.
- Morfitt, J.L., Martin, W.R., François, R., Carney, C.M., 2009. A model for uranium, rhenium, and molybdenum diagenesis in marine sediments based on results from coastal locations. *Geochim. Cosmochim. Acta.* 73, 2938–2960.
- Murray, R.W., 1994. Chemical criteria to identify the depositional environment of chert: general principles and applications. *Sed. Geol.* 90, 213–232.
- Nothdurft, L.D., Webb, G.E., Kamber, B.S., 2004. Rare earth element geochemistry of Late Devonian reefal carbonates, Canning Basin, Western Australia: confirmation of a seawater REE proxy in ancient limestones. *Geochim. Cosmochim. Acta.* 68, 263–283.
- Nozaki, Y., Zhang, J., Amakawa, H., 1997. The fractionation between Y and Ho in the marine environment. *Earth Planet. Sci. Lett.* 148, 329–340.
- Poulton, S.W., 2021. The Iron Speciation Paleoredox Proxy. *Elements in Geochemical Tracers in Earth System Science*. Cambridge University Press.
- Poulton, S.W., Canfield, D.E., 2005. Development of a sequential extraction procedure for iron: implications for iron partitioning in continentally derived particulates. *Chem. Geol.* 214, 209–221.
- Poulton, S.W., Canfield, D.E., 2011. Ferruginous Conditions: A Dominant Feature of the Ocean through Earth's History. *Elements* 7, 107–112.
- Ramseyer, K., Amthor, J.E., Matter, A., Pettke, T., Wille, M., Fallick, A.E., 2013. Primary silica precipitate at the Precambrian/Cambrian boundary in the South Oman Salt Basin, Sultanate of Oman. *Mar. Petrol. Geol.* 39, 187–197.
- Reddy, T.R., Zheng, X.-Y., Roden, E.E., Beard, B.L., Johnson, C.M., 2016. Silicon isotope fractionation during microbial reduction of Fe(III)-Si gels under Archean seawater conditions and implications for iron formation genesis. *Geochim. Cosmochim. Acta.* 190, 85–99.
- Schijf, J., Byrne, R.H., 2021. Speciation of yttrium and the rare earth elements in seawater: Review of a 20-year analytical journey. *Chem. Geol.* 584, 120479.
- Shibata, N., Furukawa, N., Kubota, M., 1993. Oxide formation in electrothermal vaporization inductively coupled plasma mass spectrometry. *Spectrochim. Acta, Part B* 48, 1127–1137.
- Shields, G., Stille, P., 2001. Diagenetic constraints on the use of cerium anomalies as palaeoseawater redox proxies: an isotopic and REE study of Cambrian phosphorites. *Chem. Geol.* 175, 29–48.
- Shields-Zhou, G., Zhu, M., 2013. Biogeochemical changes across the Ediacaran–Cambrian transition in South China. *Precambrian Res.* 225, 1–6.
- Sholkovitz, E.R., Landing, W.M., Lewis, B.L., 1994. Ocean particle chemistry: the fractionation of rare earth elements between suspended particles and seawater. *Geochim. Cosmochim. Acta.* 58, 1567–1579.
- Siever, R., 1992. The silica cycle in the Precambrian. *Geochim. Cosmochim. Acta.* 56, 3265–3272.
- Slack, J.F., Grenne, T., Bekker, A., Rouxel, O.J., Lindberg, P.A., 2007. Suboxic deep seawater in the late Paleoproterozoic: Evidence from hematitic chert and iron formation related to seafloor-hydrothermal sulfide deposits, central Arizona, USA. *Earth Planet. Sci. Lett.* 255, 243–256.
- Soyol-Erdene, T.-O., Huh, Y., 2013. Rare earth element cycling in the pore waters of the Bering Sea Slope (IODP Exp. 323). *Chem. Geol.* 358, 75–89.
- Stolper, D.A., Love, G.D., Bates, S., Lyons, T.W., Young, E., Sessions, A.L., Grotzinger, J.P., 2017. Paleoecology and paleoceanography of the Athel silicicarbonate, Ediacaran–Cambrian boundary, Sultanate of Oman. *Geobiology* 15, 401–426.
- Sun, Y., Ouyang, Q., Lang, X., Pang, K., Wu, C., Chen, Z., Zhou, C., 2023. Global sea-level fall triggered Ediacaran–Cambrian unconformity in North China craton. *Earth Planet. Sci. Lett.* p. 622.
- Tatzel, M., von Blanckenburg, F., Oelze, M., Bouchez, J., Hippler, D., 2017. Late Neoproterozoic seawater oxygenation by siliceous sponges. *Nat. Commun.* 8, 621.
- Tostevin, R., Shields, G.A., Tarbuck, G.M., He, T., Clarkson, M.O., Wood, R.A., 2016. Effective use of cerium anomalies as a redox proxy in carbonate-dominated marine settings. *Chem. Geol.* 438, 146–162.
- Tréguer, P.J., Sutton, J.N., Brzezinski, M., Charette, M.A., Devries, T., Dutkiewicz, S., Ehler, C., Hawkins, J., Leynaert, A., Liu, S.M., 2021. Reviews and syntheses: The biogeochemical cycle of silicon in the modern ocean. *Biogeosciences* 18, 1269–1289.
- Tribouillard, N., Algeo, T.J., Lyons, T., Ribouleau, A., 2006. Trace metals as paleoredox and paleoproduction proxies: An update. *Chem. Geol.* 232, 12–32.
- Van der Meer, D.G., van den Berg van Saparoea, A.P.H., van Hinsbergen, D.J.J., van de Weg, R.M.B., Godderis, Y., Le Hir, G., Donnadieu, Y., 2017. Reconstructing first-order changes in sea level during the Phanerozoic and Neoproterozoic using strontium isotopes. *Gondwana Research* 44, 22–34.
- Van der Weijden, C.H., 2002. Pitfalls of normalization of marine geochemical data using a common divisor. *Mar. Geol.* 184, 167–187.

- Wang, J., Chen, D., Wang, D.A.N., Yan, D., Zhou, X., Wang, Q., 2011. Petrology and geochemistry of chert on the marginal zone of Yangtze Platform, western Hunan, South China, during the Ediacaran–Cambrian transition. *Sedimentology* 59, 809–829.
- Wang, D., Struck, U., Ling, H.-F., Guo, Q.-J., Shields-Zhou, G.A., Zhu, M.-Y., Yao, S.-P., 2015. Marine redox variations and nitrogen cycle of the early Cambrian southern margin of the Yangtze Platform, South China: evidence from nitrogen and organic carbon isotopes. *Precambrian Res.* 267, 209–226.
- Wang, Y., Wignall, P.B., Xiong, Y., Loydell, D.K., Peakall, J., Baas, J.H., Mills, B.J.W., Poulton, S.W., 2024. Marine redox dynamics and biotic response to the mid-Silurian Ireviken Extinction Event in a mid-shelf setting. *J. Geol. Soc.*, p. 181.
- Wang, Z.H., Xie, X.M., We, Z.G., 2022. Formation conditions of Ediacaran–Cambrian cherts in South China: Implications for marine redox conditions and paleoecology. *Precam. Res.* 383, 106867.
- Webb, G.E., Kamber, B.S., 2000. Rare earth elements in Holocene reefal microbialites: a new shallow seawater proxy. *Geochi. Cosochi. Acta*. 64, 1557–1565.
- Wei, W., Frei, R., Gilleadeau, G.J., Li, D., Wei, G.-Y., Huang, F., Ling, H.-F., 2020. Variations of redox conditions in the atmosphere and Yangtze Platform during the Ediacaran–Cambrian transition: Constraints from Ce isotopes and Ce anomalies. *Palaeogeogr., Palaeoclimatol., Palaeoecol.* 543, 109598.
- Wei, G.Y., Zhao, M., Sperling, E.A., Gaines, R.R., Kalderon-Asael, B., Shen, J., Li, C., Zhang, F., Li, G., Zhou, C., Cai, C., Chen, D., Xiao, K.Q., Jiang, L., Ling, H.F., Planavsky, N.J., Tarhan, L.G., 2024. Lithium isotopic constraints on the evolution of continental clay mineral factory and marine oxygenation in the earliest Paleozoic Era. *Sci. Adv.* 10, eadk2152.
- Wu, Y., Tian, H., Jia, W., Li, J., Li, T., Zhou, Q., Xie, L., Peng, P.A., 2022. Nitrogen isotope evidence for stratified ocean redox structure during late Ediacaran to Cambrian Age 3 in the Yangtze Block of South China. *Chem. Geol.* 589.
- Xue, Y., Zhou, C., 2006. Resedimentation of the Early Cambrian phosphatized small shell fossils and correlation of the Sinian–Cambrian boundary strata in the Yangtze Region, southern China. *J. Stratigraphy* 30, 64–74.
- Yamamoto, K., 1987. Geochemical characteristics and depositional environments of cherts and associated rocks in the Franciscan and Shimanto Terranes. *Sed. Geol.* 52, 65–108.
- Yang, H., Yang, L., Zhou, M., 2022. Expanded deepwater euxinia recorded in the Ediacaran–Cambrian boundary interval in South China. *J. Asian Earth Sci.* 230.
- Ye, Y., Frings, P.J., von Blanckenburg, F., Feng, Q., 2021. Silicon isotopes reveal a decline in oceanic dissolved silicon driven by biosilicification: A prerequisite for the Cambrian Explosion? *Earth Planet. Sci. Lett.*, p. 566.
- Yu, B., Dong, H., Widom, E., Chen, J., Lin, C., 2009. Geochemistry of basal Cambrian black shales and cherts from the Northern Tarim Basin, Northwest China: Implications for depositional setting and tectonic history. *J. Asian Earth Sci.* 34, 418–436.
- Zepeda, V.K., Kamber, B.S., Ghidan, O.Y.A., 2024. Direct accurate Eu anomaly analysis in very high Ba/Eu silicate samples by triple-quadrupole ICP-MS in MS/MS mass shift mode. *Chem. Geol.*, p. 647.
- Zhang, Y., Feng, Q., Nakamura, Y., Suzuki, N., 2021b. Microfossils from the Liuchapo Formation: Possible oldest radiolarians from deep-water chert and phylogenetic analysis. *Precambrian Res.* 362.
- Zhang, S., Li, H., Jiang, G., Evans, D.A.D., Dong, J., Wu, H., Yang, T., Liu, P., Xiao, Q., 2015. New paleomagnetic results from the Ediacaran Doushantuo Formation in South China and their paleogeographic implications. *Precambrian Res.* 259, 130–142.
- Zhang, K., Zhu, X., Wood, R.A., Shi, Y., Gao, Z., Poulton, S.W., 2018. Oxygenation of the Mesoproterozoic ocean and the evolution of complex eukaryotes. *Nat. Geosci.* 11, 345–350.
- Zhang, K., Li, X., Wang, Y., Liu, W., Yu, Y., Zhou, L., Feng, W., 2021a. Paleo-environments and organic matter enrichment in the shales of the Cambrian Niutitang and Wunitang Formations, south China: Constraints from depositional environments and geochemistry. *Mar. Petrol. Geol.*, p. 134.
- Zhang, K., Shields, G.A., 2022. Sedimentary Ce anomalies: Secular change and implications for paleoenvironmental evolution. *Earth-Sci. Rev.*, p. 229.
- Zheng, Y., Anderson, R.F., Van Geen, A., Kuwabara, J., 2000. Authigenic molybdenum formation in marine sediments: a link to pore water sulfide in the Santa Barbara Basin. *Geochi. Cosochi. Acta*. 64, 4165–4178.
- Zheng, Y., Anderson, R.F., van Geen, A., Fleisher, M.Q., 2002. Preservation of particulate non-lithogenic uranium in marine sediments. *Geochi. Cosochi. Acta*. 66, 3085–3092.
- Zheng, X.-Y., Beard, B.L., Reddy, T.R., Roden, E.E., Johnson, C.M., 2016. Abiologic silicon isotope fractionation between aqueous Si and Fe (III)-Si gel in simulated Archean seawater: Implications for Si isotope records in Precambrian sedimentary rocks. *Geochi. Cosochi. Acta*. 187, 102–122.
- Zhu, M.Y., Zhuravlev, A.Y., Wood, R., Zhao, F., Sukhov, S., 2017. A deep root for the Cambrian explosion: Implications of new bio-and chemostratigraphy from the Siberian Platform. *Geology* 45, 459–462.